# A General Mechanism for Initiating the General Stress Response in Bacteria

Rishika Baral[1,2], Kristin Ho[1], Ramasamy P. Kumar[1], Jesse B. Hopkins[3], Maxwell B. Watkins[4], Salvatore LaRussa[1,2], Suhaily Caban-Penix[1,5], Logan A. Calderone[1,2], and Niels Bradshaw[1*]

[1]Department of Biochemistry, Brandeis University, Waltham, Massachusetts, USA

[2]Graduate program in Biochemistry and Biophysics, Brandeis University, Waltham, Massachusetts, USA

[3]Biophysics Collaborative Access Team (BioCAT), Department of Physics, Illinois Institute of Technology, Chicago, Illinois, USA

[4]Biophysics Collaborative Access Team (BioCAT), Department of Biology, Illinois Institute of Technology, Chicago, Illinois, USA

[5]Graduate program in Molecular and Cell Biology, Brandeis University, Waltham, Massachusetts, USA

[*]To whom correspondence should be addressed: niels@brandeis.edu

## Abstract

The General Stress Response promotes survival of bacteria in adverse conditions, but how sensor proteins transduce species-specific signals to initiate the response is not known. The serine/threonine phosphatase RsbU initiates the General Stress Response in *B. subtilis* upon binding a partner protein (RsbT) that is released from sequestration by environmental stresses. We report that RsbT activates RsbU by inducing otherwise flexible linkers of RsbU to form a short coiled-coil that dimerizes and activates the phosphatase domains. Importantly, we present evidence that related coiled-coil linkers and phosphatase dimers transduce signals from diverse

sensor domains to control the General Stress Response and other signaling across bacterial phyla. This coiled-coil linker transduction mechanism additionally suggests a resolution to the mystery of how shared sensory domains control serine/threonine phosphatases, diguanylate cyclases and histidine kinases. We propose that this provides bacteria with a modularly exchangeable toolkit for the evolution of diverse signaling pathways.

## Introduction

The General Stress Response (GSR) allows bacteria to survive in hostile and changing environments(Bergkessel et al. 2016; Harms et al. 2016; Gottesman 2019; Guldimann et al. 2016; Hecker et al. 2007). A defining feature of the GSR is that it controls transcription of a large and diverse set of genes, dramatically reshaping the physiology of the organism (Gottesman 2019; Guerreiro et al. 2020; Boekhoud et al. 2020; Boylan et al. 1993). Another defining feature is that the GSR is induced by a variety of stress conditions that are frequently associated with each other, including stationary phase, nutrient depletion, cellular damage, and (for pathogens) host defense mechanisms (Gottesman 2019). This multiplicity of initiating conditions allows cells to anticipate and prepare for accumulating adversity, suggesting why the GSR is present in every bacterial species that has so far been analyzed. The GSR additionally contributes to pathogenesis through expression of genes controlling virulence, biofilm formation, and quorum sensing (Kint et al. 2017; Battesti et al. 2015; Bartolini et al. 2019). Inactivation of the GSR, in turn, promotes the transition to long-term slow growth and antibiotic resistance, which are particularly important for persistent infections (Tuchscherr & Löffler 2016; Herbert et al. 2010; Bergkessel et al. 2016). Thus, deciphering the mechanisms that govern GSR activity is critical to understanding how bacteria interact with and adapt to their environments.

A major barrier to understanding initiation of the GSR is that we lack a unique, generalizable mechanistic model for how the activating signaling proteins have evolved to respond to species-specific signals. In a widespread mechanism for initiating the GSR, a member of the PPM family of serine/threonine phosphatases dephosphorylates a phosphorylated substrate protein to activate an alternative σ-factor through a "partner-switching" mechanism (Hecker et al. 2007), but how the phosphatase receives and is activated by an upstream signal has not been determined.

In this study, we address how the GSR phosphatase RsbU from *B. subtilis* is regulated (Yang et al. 1996) and present evidence that this mechanism is widely conserved. RsbU dephosphorylates a single phospho-serine on its substrate protein (RsbV) to release the GSR transcription factor ($\sigma^B$) from inhibition by an anti-sigma factor (RsbW) (Figure 1A). RsbU has an N-terminal four-helix bundle domain that dimerizes RsbU and is also the binding site for RsbT, which activates RsbU as a phosphatase (Figure 1C,D) (Delumeau et al. 2004). RsbT is sequestered in a megadalton stress sensing complex called the stressosome, and is released to bind RsbU in response to specific stress signals including ethanol, heat, acid, salt, and blue light (Hecker et al. 2007; Marles-Wright et al. 2008). We and others have reconstituted RsbU activation by RsbT (Delumeau et al. 2004; Ho & Bradshaw 2021), but how RsbT activates RsbU was not known.

This "partner-switching" mechanism is broadly conserved, and the activating phosphatases are observed to have diverse N-terminal sensory domains including PAS (Vijay et al. 2000; Greenstein et al. 2009; Fernández Martínez et al. 2009), response-receiver (de Been et al. 2010; Rodríguez-Martínez et al. 2023), GAF (Kint et al. 2019), and HAMP (Mittenhuber 2002). These

signaling domains are frequently found as N-terminal regulators of histidine kinases and GGDEF diguanylate cyclases in bacteria, but whether or not there are shared mechanistic features between the regulatory principles of PPM phosphatases and these other signaling effector families is not known (Möglich et al. 2009; Galperin 2006).

We previously described a mechanism for allosteric control of the related *B. subtilis* phosphatase SpoIIE, which regulates endospore formation through a partner-switching mechanism analogous to RsbU control of the GSR (Ho & Bradshaw 2021; Bradshaw et al. 2017). Two helices of the PPM domain (α1 and α2), which we refer to as the switch element, change conformation to recruit metal cofactor and activate SpoIIE (Bradshaw et al. 2017). Based on analysis of structural and genetic data, we conjectured that this conformational change exemplifies a common mechanism among diverse phosphatases. However, we could not propose a specific model for how unrelated regulatory domains modularly control the switch conformation. For RsbU, we found that RsbT enhances phosphatase activity by increasing the efficacy of metal cofactor binding and that substitution of an amino acid in α1 ($RsbU^{M166V/L}$) activates RsbU in the absence of RsbT (Ho & Bradshaw 2021) These results supported our proposal that the switch element controls RsbU activation, but they did not reveal how RsbT binding to the N-terminus of RsbU is transduced to the switch.

One broadly conserved feature of GSR phosphatases (absent in SpoIIE) is an α-helical linker of variable length, which is N-terminal to the PPM phosphatase domain. Genetic data suggest that this linker regulates a paralogous *B. subtilis* GSR phosphatase (RsbP) (Brody et al. 2009). Here we report that binding of RsbT to the N-terminus of RsbU rigidifies an otherwise flexible linker

to dimerize the C-terminal phosphatase domains through an interface mediated by the switch element. Importantly, and as we now report, this mechanism is generalizable to other PPM phosphatases and reveals a widespread feature of bacterial signaling.

## Results

### The linker controls RsbU activation through a predicted phosphatase dimer

We previously conducted a genetic screen (Ho & Bradshaw 2021) to identify features of RsbU that are important for phosphatase regulation by isolating gain-of-function variants that are active in the absence of RsbT. Focusing on the phosphatase domain in our initial study, we reported identification of an amino acid substitution in α1 ($RsbU^{M166V/L}$) that links the switch element to RsbU activation (Ho & Bradshaw 2021). From this screen, we isolated a second variant, $RsbU^{Q94L}$, located in the linker of RsbU between the N-terminal dimerization domain and the C-terminal phosphatase domain (Figure 1B-D). *rsbU*$^{Q94L}$ strains activated $\sigma^B$ in the absence of *rsbT*. This activation is comparable to when *rsbT* is overexpressed to exceed the capacity of the stressosome and is stronger than what we observe in strains expressing *rsbU*$^{M166V/L}$ (Figure 1B).

To visualize how the Q94L and M166V/L substitutions could impact RsbU structure and activity, we generated an AlphaFold2 model of an RsbU dimer (Jumper et al. 2021; Mirdita et al. 2022) (Figure. 1D). The prediction of the complex was of high confidence (Figure 1- figure Supplement 1-2) and had a dimer of the N-terminal region consistent with a previous experimental structure (Delumeau et al. 2004). In our model, the linkers form extended alpha-helices (82-112) that cross to connect dimers of the RsbU N-terminal domains and C-terminal

phosphatase domains, with Q94 buried in the linker interface and M166 buried in the core of the phosphatase domain (Figure 1D).

The crossing linker helices have similar conformation to homologous linkers observed in crystal structures of *P. aeruginosa* RssB, a phosphatase/adapter protein that also controls the GSR (PDB 3F7A and 3EQ2, Figure 1 – Figure Supplement 3). RssB has an N-terminal response-receiver domain in place of the RsbU four helix bundle dimerization domain, suggesting that linker conformation is a conserved feature of PPM phosphatase dimers with divergent N-terminal regulatory domains (Figure 1 – Figure Supplement 3). The linker helices in the RsbU prediction and the RssB structure splay apart as they enter the PPM domain with similar angle (pitch angles (α) based on Crick parameters for coiled-coils –17.6º and –18.4º respectively) and pack against α-1 of the PPM fold (Grigoryan & DeGrado 2011). Interestingly, we observed that other bacterial signaling proteins that are regulated by coiled-coil linkers had similar pitch angle for the helices connecting to the catalytic domains (for example the dimeric histidine kinase CheA, 1B3Q, α –16.8º, and the dimeric GGDEF diguanylate cyclase PadC, 5LLW, α –14.3º) (Bilwes et al. 1999; Gourinchas et al. 2017; Grigoryan & DeGrado 2011) (Figure 1 – Figure Supplement 3). Thus, the linker of RsbU could be a conserved regulatory feature, analogous to linkers of histidine kinases and GGDEF diguanylate cyclases.

Analysis of the RsbU dimer model using Socket2 identifies amino acids 83-97 as a two-turn coiled coil, with Q94 unfavorably packing against leucine 90 (Kumar & Woolfson 2021) (Figure 1 – Figure Supplement 3). To test whether hydrophobicity at position 94 promotes an active state, we tested the activity of RsbU alleles with different amino acid substitutions at position 94

139 for $\sigma^B$ in wildtype and *rsbT* deleted strains. We found that substitutions of Q94 with amino acids
140 that could pack at the intersection of the crossing linker helices (hydrophobic residues isoleucine,
141 valine, and methionine, as well as tyrosine) resulted in mild, RsbT-independent activation of $\sigma^B$
142 that was further heightened by RsbT (Figure 1 – Figure Supplement 3). Aromatic hydrophobic
143 residues (phenylalanine and tryptophan) drove constitutive activation of RsbU but did not bypass
144 the requirement for *rsbT* on the chromosome (Figure 1 – Figure Supplement 1). Substitutions of
145 small or charged residues (alanine, glycine, glutamate, and asparagine) did not lead to activity in
146 either strain (Figure 1 – Figure Supplement 3). These results are consistent with a model in
147 which burial of the amino acid at position 94, such as in the crossed helices of our prediction for
148 RsbU dimer structure, drives RsbU activation.
149
150 **RsbT binding to RsbU is influenced by the linker**
151 One prediction of our hypothesis that RsbT stabilizes the crossed alpha helices of the RsbU
152 dimer, is that RsbT should bind more tightly to $RsbU^{Q94L}$ than to RsbU because the coiled-coil
153 conformation that RsbT binds would be more energetically favorable. To test this, we measured
154 the binding affinity of RsbT for RsbU using fluorescence anisotropy. From these data we
155 obtained a $K_D$ of 4.5 ± 1 μM, which decreased approximately 10-fold for $RsbU^{Q94L}$ (0.56 ± 0.2
156 μM) (Figure 2A). Thus, $RsbU^{Q94L}$ stimulates RsbU phosphatase activity by an on-pathway
157 mechanism, supporting the idea that RsbT binding stabilizes the linker in a dimerized
158 conformation to activate RsbU.
159
160 **RsbU phosphatase activation is controlled by the linker**

161 We previously found that RsbT activates RsbU by simultaneously decreasing the $K_M$ for
162 manganese cofactor and increasing the $k_{cat}$ for dephosphorylation of RsbV-P (Ho & Bradshaw
163 2021). To test whether RsbU Q94L substitution works by the same kinetic mechanism, we
164 measured dephosphorylation of $^{32}$P-phosphorylated RsbV by $RsbU^{Q94L}$ (Figure 2B). The $k_{cat}$ of
165 $RsbU^{Q94L}$ was nearly the same as for the basal activity of RsbU (2.4 ± 0.1 $min^{-1}$ compared to 1.4
166 ± 0.1 $min^{-1}$, and stimulated more than ten-fold by RsbT, 15 ± 0.4 $min^{-1}$) (Figure 2B) (Ho &
167 Bradshaw 2021). However, $RsbU^{Q94L}$ had a $K_M$ for $MnCl_2$ (1.4 ± 0.2 mM) that is more than fifty-
168 fold reduced compared to RsbU alone (77 ± 9 mM) (Ho & Bradshaw 2021), and similar to the
169 $K_M^{MnCl2}$ of RsbU in the presence of RsbT (0.98 ± 0.07 mM (Ho & Bradshaw 2021)) (Figure 2B).
170 Addition of RsbT did not change the $K_M$ of $RsbU^{Q94L}$ for $MnCl_2$ (1.9 ± 0.6 mM), but the
171 maximum catalytic rate of dephosphorylation increased nearly four-fold to 9.0 ± 0.64 $min^{-1}$,
172 approaching the rate of RsbU stimulated by RsbT (Figure 2B). Thus, $RsbU^{Q94L}$ substantially
173 recapitulates RsbT activation by decreasing the $K_M$ for $Mn^{2+}$, demonstrating that the linker
174 transduces RsbT binding to control the active site of RsbU (Figure 2C). This is consistent with
175 previous findings that the allosteric switch controlling phosphatase activity of SpoIIE couples
176 dimerization to cofactor interaction.
177

178 **RsbT binds to the linker and N-terminal domain**

179 To visualize how RsbT could control the linker to activate RsbU, we generated an AlphaFold2
180 prediction of a heterotetrameric complex between RsbT and RsbU (Figure 3A). In this model,
181 RsbU adopts a conformation very similar to our prediction of the RsbU dimer (RMSD 1.36 Å),
182 suggesting that our AlphaFold2 RsbU dimer model represents the active state of RsbU even
183 when RsbT was not included in the prediction (a known feature of AlphaFold2

models(Chakravarty & Porter 2022). The predicted structure places RsbT in a hybrid interface that spans the N-terminal dimerization domain of both RsbU monomers and the linker of one monomer (Figure 3A). Supporting the validity of the AlphaFold2 2RsbT/2RsbU model, residues previously implicated in RsbT/U binding (Hardwick et al. 2007) (Y28 and E24 from one RsbU monomer, I74, and I78 from the other RsbU monomer, and RsbT R19, R23, and N24) are all buried in the predicted interface (Figure 3 – Figure supplement 1).

To gain further insight into how RsbT binding is transduced to RsbU linker conformation and phosphatase activity, we performed a genetic screen to isolate suppressors of $RsbU^{Y28I}$, which was previously observed to abolish binding to RsbT (Hardwick et al. 2007). After screening a library of PCR mutagenized $rsbU^{Y28I}$ and *rsbT*, we identified eleven variants that introduced substitutions to RsbU that suppress $rsbU^{Y28I}$: S49G, K53E, T89A, G92E, G92R, Q94L, T110S, V142A, K143E, C165Y, and M173I (Figure 3A-B). We additionally isolated revertants that restored Y28 suggesting that the screen was near saturation, but did not isolate any suppressors in *rsbT*, which was also mutagenized.

Mapping the $RsbU^{Y28I}$ suppressor mutations onto our 2RsbU/2RsbT model suggests that they fall into three classes (Figure 3A and B): *(1)* Substitutions in the RsbU N-terminal dimerization domain that map near the predicted RsbT binding site (S49G and K53E), supporting the predicted interface. *(2)* Substitutions that map near predicted contacts between RsbT and the RsbU linker (T89A, G92E/R, and Q94L), providing evidence that contacts between RsbT and the linker promote RsbU activation. *(3)* Substitutions that cluster around the regulatory switch element of the RsbU phosphatase domain (helices α1 and α2 of the PPM fold, T110S, V142A,

K143E, C165Y, and M173I). We hypothesize that these substitutions rescue $RsbU^{Y28I}$ inactivation by reducing the energetic cost (normally provided by RsbT binding) to transition the RsbU phosphatase domain to the active conformation. Together these genetic data provide independent support for the AlphaFold2 model of the 2RsbT/2RsbU complex, and suggest that RsbT activates RsbU by transmitting signals to the switch element in the RsbU phosphatase domain through a coiled-coil linker.

**Contacts between RsbT and the RsbU linker drive phosphatase activation**

To test the model that RsbT activates RsbU by directly interacting with the linker to dimerize the RsbU phosphatase domains, we introduced a charge swap at position R91 that would abolish a predicted salt-bridge with RsbT D92 (Figure 3C). $RsbU^{R91E}$ abolished $\sigma^B$ activity for cells overexpressing *rsbT* (Figure 3C), and in biochemical assays RsbT stimulation of $RsbU^{R91E}$ phosphatase activity was abolished (Figure 3D). Finally, we introduced a potentially compensatory charge switch at position D92 of RsbT ($RsbT^{D92K}$) (Figure 3C). Expression of $rsbT^{D92K}$ partially restored $\sigma^B$ activity to $rsbU^{R91E}$ expressing cells, consistent with direct interaction between these residues (Figure 3C). Together, these results suggest that contacts between RsbT and the linker of RsbU are responsible for phosphatase activation.

**The RsbU linker is flexible in the absence of RsbT**

We considered two models for why RsbU is inactive in the absence of RsbT. One possibility is that inactive RsbU resembles the dimeric structure predicted by AlphaFold2 and that RsbT induces a subtle conformational change, for example changing the registry or pitch of the crossing linker helices. A second possibility is that inactive RsbU is dimerized by the N-terminal

230 domains but that the linkers of inactive RsbU are flexible and that the phosphatase domains only
231 interact with each other when RsbT orders the linkers into a crossing conformation. To
232 distinguish between these two models, we performed small angle X-ray scattering coupled to
233 size exclusion chromatography with multi-angle light scattering (SEC-MALS-SAXS) to assess
234 the shape and flexibility of RsbU dimers in solution (Table 1 and Figure 4 – Figure Supplement
235 1-2 S4A). RsbU eluted as a single peak from the size exclusion column with an average
236 molecular weight of 77 kDa (calculated dimeric molecular weight 77.3 kDa) determined by
237 multi-angle light scattering (MALS) (Figure 4 – Figure Supplement 1). However, our sample had
238 a minor contaminant of heterodimeric complexes of RsbU in which one monomer is C-
239 terminally truncated that could influence the SAXS analysis (Figure 4 – Figure Supplement 1).
240 We therefore deconvoluted the SAXS profiles using evolving factor analysis (EFA) in RAW to
241 isolate scattering profiles from the individual components (Hopkins et al. 2017; Meisburger et al.
242 2016) (Figure 4 – Figure Supplement 2).The EFA deconvolution identified a major component
243 (MW 75.6 kDa calculated from $V_c$ method), which eluted earlier than a smaller component (MW
244 48.8 kDa calculated from $V_c$ method) (Table 1 Guinier fits, and Figure 4 – Figure Supplement 2).
245 We conclude that the larger component is a RsbU dimer, while the smaller fragment is likely a
246 heterodimeric complex of RsbU and the C-terminal truncation product of RsbU (Figure 4 –
247 Figure Supplement 1).
248
249 Indicative of significant deviation between the RsbU structure in solution to the AlphaFold2
250 model, the scattering intensity profile (I(q) vs. q) was a poor fit ($\chi^2$ 12.53) to a profile calculated
251 from the AlphaFold2 model of an RsbU dimer using FoXS (Schneidman-Duhovny et al. 2016;
252 Schneidman-Duhovny et al. 2013) (Figure 4A). We therefore assessed the SAXS data for the

253 RsbU dimer for features that report on flexibility (Kikhney & Svergun 2015). First, the scattering
254 intensity data lacked distinct features caused by the multi-domain structure of RsbU from the
255 AlphaFold2 model (Figure 4A). This can be visualized more readily from a dimensionless
256 Kratky plot, which is bell-shaped and peaks above 1.3, indicating that the RsbU dimer is non-
257 globular (Figure 4B). Additionally, the data do not show the two peaks from the FoXS computed
258 model of the AlphaFold2 dimer that reflect the extended two domain structure (Kikhney &
259 Svergun 2015; Receveur-Bréchot & Durand 2012) (Figure 4 – Figure Supplement 2). The
260 scattering data had several additional characteristic features indicating flexibility: the P(r) plot is
261 smooth and has an extended tail (Cordeiro et al. 2017; Kikhney & Svergun 2015; Receveur-
262 Bréchot & Durand 2012) (Figure 4C), $R_g$ and I(0) calculated from P(r) are larger than when
263 calculated from Guinier fits (Cordeiro et al. 2017; Kikhney & Svergun 2015; Receveur-Bréchot
264 & Durand 2012) (Table 1), molecular weight calculated using the MoW2 modified Porod
265 volume method is an overestimate (Rambo & Tainer 2011) (Table 1), and the $R_g$ (39.05 ± 0.16
266 Å) was larger than the $R_g$ of the AlphaFold2 dimer model (34.05 Å). Prompted by this evidence
267 of flexibility, we performed multi-state modelling using MultiFoXS (Schneidman-Duhovny et al.
268 2016), which incorporates flexibility and heterogeneity. MultiFoXS produced a two-state
269 solution with $\chi^2$ of 1.2 (as compared to the one-state model with $\chi^2$ of 12.5) and low residuals
270 across the entire range of data (Figure 4D, Figure 4 – Figure Supplement 2). We allowed
271 flexibility for the linker residues 82-96 while keeping the N-terminal domain dimerized because
272 a stable dimer of the N-terminal domain is observed in solution, was present in a previous X-ray
273 crystal structure of C-terminally truncated RsbU{Delumeau:2004ep}, and C-terminally truncated
274 RsbU coelutes as a heterodimer with the full-length protein (Figure 4 – Figure Supplement 1).
275 Importantly, the precise region of allowed linker flexibility does not have a substantial impact on

276 the MultiFoXS fit (Figure 4 – Figure Supplement 3), but constraining the C-terminal phosphatase
277 domain dimer does not yield a good fit to the data ($\chi^2$ of 5.4) (Figure 4 – Figure Supplement 3).
278 The structural models predicted by MultiFoXS depict a dimerized N-terminal domain with
279 flexible linkers and PPM domains that do not make contact. Notably, this approach also would
280 include models in which both domains remain dimerized, suggesting that such models are not the
281 best fit of the data. The two conformations that were selected as the best fit to the scattering data
282 by MultiFoXS also have very different $R_g$ values, (34.91 Å (71%) and 45.69 Å (29%)),
283 indicating RsbU samples a range of conformational space that includes a more compact state(s)
284 consistent with the AlphaFold2 model and a significantly extended state(s), emphasizing that the
285 linker is highly flexible. Together, we conclude that the RsbU linker appears to be flexible in the
286 absence of RsbT (Figure 4G).
287
288 **RsbT rigidifies and compacts the RsbU dimer**
289 To test the hypothesis that RsbT rigidifies the linker to produce an active RsbU dimer, we
290 attempted SEC-MALS-SAXS analysis of the RsbT/U complex. RsbT/U eluted with molecular
291 weight (determined by MALS) of 88 kDa compared to 105 kDa for a 2RsbT/2RsbU
292 heterotetramer (Figure 4 – Figure Supplement 1), suggesting that the RsbT/U complex had
293 largely disassembled on the column. We therefore performed SEC-MALS-SAXS on the
294 RsbT/RsbU$^{Q94L}$ complex, which has a higher affinity (Figure 2A, Figure 4 - Figure Supplement
295 4). The RsbT/U$^{Q94L}$ complex eluted as a major peak with a higher molecular weight shoulder
296 (Figure 4 - Figure Supplement 1, 4) (also visible when we ran RsbU$^{Q94L}$ alone. Figure 4 – Figure
297 Supplement 1), with the average molecular weight of the main peak (determined by MALS) of
298 125 kDa (Figure 4 – Figure Supplement 1). This is larger than the predicted molecular weight of

299 a heterotetrameric 2RsbT/2RsbU$^{Q94L}$ complex (105 kDa), suggesting that some higher order
300 complexes form. EFA deconvolution (Meisburger et al. 2016) identifies two components. The
301 first deconvolved component had a SAXS determined molecular weight of 164 kDa, while the
302 second had a SAXS molecular weight of 103 kDa, consistent with a 2RsbT/2RsbU complex (105
303 kDa). Together with the fact that RsbT co-elutes with RsbU$^{Q94L}$ throughout the entire peak
304 (Figure 4 – Figure Supplement 1) and the MALS molecular weight, we assess that this second
305 component is an 2RsbT/2RsbU hetero-tetramer. The identity of the higher molecular weight
306 component of the scattering data is ambiguous, but could represent a larger assembly of
307 RsbT/RsbU$^{Q94L}$ or multimers of RsbU$^{Q94L}$ that were observed when RsbU$^{Q94L}$ was analyzed
308 alone (Figure 4 – Figure Supplement 1). Several lines of evidence demonstrate that the
309 2RsbT/2RsbU$^{Q94L}$ complex lacks the flexibility of the 2RsbU complex. First, the $R_g$ from the
310 Guiner fit (35.06 ± 0.43 Å) matches well with the model computed from the AlphaFold2
311 prediction of the heterotetrameric complex of 2RsbT/2RsbU using FoXS (33.68 Å) and is
312 smaller than the $R_g$ we observed for the RsbU dimer (39.05 ± 0.16 Å). Second, the features of the
313 scattering data that suggested flexibility for RsbU dimers all suggest that the RsbT/RsbU
314 complex is more rigid (the quality of the FoXS fit, a lower peak of the dimensionless Kratky
315 plot, and a shorter tail of the P(r) plot) (Cordeiro et al. 2017; Kikhney & Svergun 2015;
316 Receveur-Bréchot & Durand 2012) (Figure 4C,4E-4F, Figure 4 – Figure Supplement 4). Third,
317 fitting the scattering profile (I(q) vs. q) to the AlphaFold2 model yielded a $\chi^2$ of 1.83 without
318 requirement for flexibility (Figure 4E). As expected, based on the lack of evidence of flexibility
319 in the scattering profile and P(r) function, the model is not improved by the use of multi-state
320 modeling by MultiFoXS, which was run as a control (Schneidman-Duhovny et al. 2016) (Figure
321 4 - Figure Supplement 4). Together, these data support the validity of the AlphaFold2 model of

322 the heterotetrameric 2RsbT/2RsbU complex, and additionally suggest that RsbT rigidifies the
323 otherwise flexible linker of RsbU to dimerize the phosphatase domains (Figure 4G). Together
324 with our biochemical data linking RsbU linker conformation to RsbT binding, metal cofactor
325 interaction, and phosphatase activity, this provides a comprehensive model for how RsbU is
326 activated (Figure 4G).
327
328 **Regulated dimerization is an evolutionarily adaptable mechanism to control bacterial**
329 **phosphatases**
330 *B. subtilis* has a second GSR-initiating PPM phosphatase, RsbP, that has an N-terminal PAS
331 domain and dephosphorylates RsbV to activate $\sigma^B$ in response to energy stress. Our AlphaFold2
332 prediction of an RsbP dimer shows an extended alpha-helical linker connecting dimeric PAS
333 domains and phosphatase domains. Like RsbU, the interface between the dimerized phosphatase
334 domains is predicted to be mediated by α1 and α2 of the phosphatase domain. We found that
335 previously identified constitutively activating mutations in RsbP (Brody et al. 2009) map to
336 similar positions as the gain-of-function mutations we identified here for RsbU in their
337 respective predicted structures, namely the interface between α1 and α2 of the phosphatase
338 domains and the linker. RsbP is activated by a partner-protein, RsbQ, that has analogous function
339 to RsbT for RsbU. An AlphaFold2 prediction of the heterotetrameric 2RsbP/2RsbQ complex
340 places the two molecules of RsbQ in a hybrid interface between the PAS domains and linkers,
341 similar to how RsbT contacts RsbU. These predictions suggest a testable hypothesis that RsbP is
342 controlled through an activation mechanism similar to that of RsbU (Figure 5A).
343

To further probe the generality of the linker-mediated phosphatase dimer we observe for RsbU, we generated AlphaFold2 predictions for dimers of other documented GSR initiating phosphatases (*C. difficile* RsbZ (N-terminal tandem GAF domains) (Fig. 5B), *S. coelicolor* OsaC (N-terminal GAF and PAS domains), and *M. tuberculosis* Rv1364c (N-terminal PAS domain, C-terminally fused to an anti-σ factor domain and an anti-anti-σ factor domain)), as well as from examples of common domain architectures of PPM phosphatases selected from InterPro (response receiver (*Streptomyces coelicolor*, MY40396.1), GAF (*Rhodococcus aetherivorans*, WP_029544106.1), and HAMP (*Synechocystis sp.*, WP_010874143.1) domains) (Figure 5 – Figure Supplement 1). In each case AlphaFold2 produced high-confidence predictions of phosphatase domains dimerized through a shared α0, α1, α2 interface, connected to dimeric N-terminal domains by crossing α-helical linkers (Figure 1 – Figure Supplement 1-2, Figure 5 – Figure Supplement 1). Consistent with a model in which the stability of the linker plays a conserved regulatory role, the AlphaFold2 models for many of the predicted structures have unfavorable polar residues buried in the coiled-coil interface (positions *a* and *d*, for which non-polar residues are most favorable) (Figure 5 – Figure Supplement 2). From this analysis, we speculate that linker-mediated phosphatase domain dimerization is an evolutionarily conserved, adaptable mechanism to control PPM phosphatase activity. This mechanistic/structural congruence provides a framework for how distantly related phosphatases can be regulated to control diverse biological processes in bacteria (Figure 5E).

## Discussion

Since the ground-breaking discovery of $\sigma^B$, the first conditionally-activated cellular transcription factor to be identified, forty-five years ago (Haldenwang & Losick 1979), a persistent

unanswered question has been how $\sigma^B$ is turned on. Here, our findings reveal how RsbU is activated as a phosphatase in the decisive step of $\sigma^B$ activation. Below, we describe how this mechanism is broadly applicable to other bacterial signaling pathways.

**RsbT activates RsbU through a conserved phosphatase dimer**

Using unbiased genetic screens, biochemical reconstitution, biophysical approaches, and structural prediction, we have discovered that RsbT activates RsbU by rigidifying an otherwise flexible linker region to allosterically activate RsbU as a phosphatase. Our structural prediction, supported by our genetic and structural data suggest that RsbU linkers assume a crossed α-helical conformation that dimerizes the phosphatase domains (Figure 4G). This dimerization activates RsbU through a conserved switch element at the dimer interface, decreasing the $K_M$ for metal cofactor and increasing the catalytic rate. Our structural predictions suggest that this is a widespread mechanism to regulate the activity of bacterial protein serine/threonine phosphatases. While RsbU activation is controlled by a flexible-to-rigid transformation of the linker, it is possible that other conformational changes of the linker could be alter the PPM dimer to control phosphatase activity through the conserved switch element.

**A general mechanism for general stress response activation**

*E. coli* and *B. subtilis* are the most extensively studied models for GSR activation (Battesti et al. 2011; Hecker et al. 2007). However, key mechanistic features of the activation mechanisms differ between the two systems. The *E. coli* GSR is initiated by stabilizing the alternative sigma factor $\sigma^S$ (RpoS) against degradation by ClpXP (Figure 5C). Under non-stressed conditions, degradation of $\sigma^S$ is mediated by the adapter protein, RssB, which is inhibited by anti-adaptors

(IraD, IraM, and IraP) and stimulated by phosphorylation on its N-terminal response-receiver domain during stress. Historically, the differences between these systems were interpreted to mean that they operate by distinct mechanistic principles. However, RssB contains a C-terminally truncated (and therefore inactive) PPM phosphatase domain, suggesting some aspects of its regulatory mechanism could be shared with RsbU (Battesti et al. 2013).

Our findings reveal that *E. coli* RssB and *B. subtilis* RsbU use three shared regulatory features to control GSR activation through their distinct downstream mechanisms. First, the positioning of analogous flexible linkers controls GSR activation by RssB and RsbU (Brugger, Schwartz, et al. 2023; Brugger, Srirangam, et al. 2023; Dorich et al. 2019). The C-terminal pseudo-phosphatase domain of RssB is joined to its N-terminal $\sigma^S$ binding response-receiver domain by a predominantly α-helical linker (termed the segmented helical linker, or SHL) of similar length to the linker of RsbU (Dorich et al. 2019). The SHL folds to occlude the $\sigma^S$ interacting face of the response-receiver domain when bound to anti-adapters, and is remodeled to promote $\sigma^S$ interaction when the response-receiver domain is phosphorylated (Brugger, Schwartz, et al. 2023; Brugger, Srirangam, et al. 2023; Dorich et al. 2019). Supporting the hypothesis that the SHL is mechanistically related to the RsbU linker, substitution of W143, the homologous residue to Q94 of *B. subtilis* RsbU, blocks regulation by IraD and IraP (Battesti et al. 2013). Second, the interface between the linker and α1 of the phosphatase domain is critical for regulation of both RssB and RsbU (Brugger, Schwartz, et al. 2023; Dorich et al. 2019). W143 packs in a hydrophobic pocket formed with the α1 helix of the pseudo-phosphatase domain of phosphorylated RssB and IraD bound RssB (Brugger, Schwartz, et al. 2023; Dorich et al. 2019). Substitution of residues in α1, including A216 (corresponding to M166 of RsbU), block

regulation of RssB by anti-adapters, underscoring the mechanistic similarity (Battesti et al. 2013). Third, conformational change of the switch helices (α1 and α2) of the phosphatase domain is of shared regulatory importance (Battesti et al. 2013). HDX experiments demonstrate that there is decreased exchange of the α1 helix of the pseudo-phosphatase domain of RssB when $\sigma^S$ is bound, suggesting that the conformational dynamics of this region are reduced by substrate recognition (Brugger, Schwartz, et al. 2023).

These striking mechanistic similarities between RssB from *E. coli* and RsbU from *B. subtilis* suggest that key regulatory features were conserved when an ancestral phosphatase lost enzymatic activity and became a dedicated adapter protein in *E. coli* and related γ-proteobacteria. Interestingly, *P. aeruginosa* has a homologue of RssB/RsbU that functions as an adapter for $\sigma^S$ degradation, yet has a catalytically active, full length phosphatase domain and resides in an operon with an *rsbV* homologue (*rssC)* (Rodríguez-Martínez et al. 2023). Crystal structures of *P. aeruginosa* RssB revealed that it forms a dimer with crossing linkers and dimerized phosphatase domains with striking similarity to the dimer predicted for RsbU (Fig. 5C, S2C). Intriguingly, adapter protein function of *P. aeruginosa* RssB requires RssC (Rodríguez-Martínez et al. 2023), and *E. coli* RssB has been observed to weakly dimerize (Dorich et al. 2019), further supporting a direct mechanistic link between phosphatase regulation and adapter protein function. While not all GSR regulatory mechanisms involve a phosphatase or adapter protein related to RsbU/RssB, these findings suggest that linker-mediated control of a PPM phosphatase is a broadly conserved mechanism for GSR initiation across bacterial phyla.

**An exchangeable toolkit for signal transduction**

Histidine kinases and GGDEF diguanylate cyclases are the two most prevalent families of bacterial signal transduction proteins. A striking feature of their regulatory mechanisms is that they are often active in dimeric complexes that are allosterically controlled by N-terminal regulatory domains that propagate signals through crossing α-helical linkers (Zschiedrich et al. 2016; Randall et al. 2022; Gourinchas et al. 2017). Our findings that the crossing α-helical linkers are structurally similar (Fig. S2C), and that shared regulatory domains (response receiver, HAMP, and PAS domains) connect phosphatase dimers by a coiled-coil linker (Figure 5A-C, Figure 5 – Figure Supplement 1) suggests that this shared allosteric regulatory architecture allows modular exchange of N-terminal domains between PPM phosphatases, histidine kinases, and GGDEF diguanylate cyclases (Figure 5D). In support of this, the RsbU N-terminal domain and RsbT were previously shown to control GGDEF diguanylate cyclase activity in *Moorella thermoacetica* (Quin et al. 2012), histidine kinases with RsbU N-terminal domains are found in operons with *rsbT* and stressosome genes in some *Proteobacteria* species (Heinz et al. 2022), and AlphaFold2 prediction of these dimeric complexes reveals coiled-coil linkers to the effector domains (Figure 5E-F). Similarly, the PAS/α/β hydrolase module that controls RsbP phosphatase activity in *B. subtilis* is found coupled to histidine kinases and GGDEF diguanylate cyclases across bacterial phyla (Nadezhdin et al. 2011).

While the specific mechanism discovered here for linker control of RsbU activity (flexibility controlled by a binding partner) is distinct from the models for linker control of histidine kinases and GGDEF diguanylate cyclases (piston shift, scissoring, and helical rotation) (Zschiedrich et al. 2016; Randall et al. 2022), the shared dimeric architecture suggests that N-terminal regulatory domains could be modularly exchanged across effector domain families (Figure 5G). Allosteric

459 control of PPM switch element conformation could theoretically be achieved by piston shift,
460 scissoring, or helical rotation. Future characterization of PPM phosphatases will be required to
461 determine how widespread linker flexibility is as a regulatory mechanism and how modularly
462 sensory domains can be exchanged across signaling effector families.
463

464 **Acknowledgements**

465 The authors thank Richard Losick, Dorothee Kern, Chris Miller, Julia Kardon, Matthew Cabeen,
466 Liz Hedstrom, Susan Lovett, Emily Stadnicki, and Maria-Eirini Pandelia for input at various
467 stages of this project. Justin Curran, LuYing Pan, Spencer Clark, Alexis Ryan, and Wendy Yang
468 additionally contributed to the research. This research was supported by startup funds to NB
469 from Brandeis University. RB was supported by T32 GM135126 and SP was supported by T32
470 GM007122. This research used resources of the Advanced Photon Source, a U.S. Department of
471 Energy (DOE) Office of Science User Facility operated for the DOE Office of Science by
472 Argonne National Laboratory under Contract No. DE-AC02-06CH11357. BioCAT was
473 supported by grant P30 GM138395 from the National Institute of General Medical Sciences of
474 the National Institutes of Health. Use of the Pilatus 3 1M detector was provided by
475 grant 1S10OD018090 from NIGMS. The content is solely the responsibility of the authors and
476 does not necessarily reflect the official views of the National Institute of General Medical
477 Sciences or the National Institutes of Health.
478

479 **Author contributions**

480 RB, conceptualization, investigation, data analysis, visualization, writing-original draft, writing-
481 review and editing. KH, PR, conceptualization, data analysis, investigation. JH, investigation,

data analysis, writing-review and editing. MW, SLR, SCP, LC, investigation. NB, conceptualization, visualization, writing-original draft, writing-review editing, and supervision.

**Figure Legends:**

**Figure 1: The linker controls RsbU activation through a conserved switch element**

**A** Reaction scheme of the RsbU dependent pathway of the environmental stress response. RsbU is activated by its partner protein RsbT (T, purple) to dephosphorylate its substrate protein RsbV-P (V-P). This initiates transcription by displacing $\sigma^B$ from inhibition by the anti-sigma factor RsbW (W). **B** Amino acid substitutions in RsbU (Q94L and M166V) cause enhanced $\sigma^B$ activity in *B. subtilis*. Strains carrying a lacZ reporter of $\sigma^B$ activity (*ctc-lacZ*) were plated on X-gal indicator plates in the presence (top) or absence (bottom) of IPTG to induce expression of the *rsbU* constructs. Strains were deleted for *rsbT* (–) or not (+). A strain overexpressing *rsbT* is indicated by oe. Plates were imaged after 24 hours of growth at 37ºC, which was shorter than the time used to visualize *lacZ* expression from the $rsbU^{M166V}$ strain previously (Ho & Bradshaw 2021). **C** Domain diagram of RsbU. The N-terminal domain of RsbU (blue) (amino acids 1-81) is joined to the α-helical linker domain (grey) (82-112), which connects it to the PPM phosphatase domain (grey box) (121-335). The regulatory switch element of the PPM phosphatase domain is colored orange (156-201). The location of RsbT-bypass mutations are highlighted in green. **D** AlphaFold2 model of RsbU dimer. Domains are colored as in **C** and the Cα atoms of residues Q94 and M166 are shown as spheres.

**Figure 2: RsbU linker influences RsbT binding and phosphatase activity**

505 **A** Mean anisotropy of RsbT-TMR (200 nM) is plotted as a function of RsbU concentration. The
506 curves are fits to a quadratic binding equation using non-linear curve fitting (RsbU (black) $K_D$ =
507 4.5 ± 0.96 μM, $RsbU^{Q94L}$ (green) $K_D$ = 0.56 ± 0.15 μM). The lower plot shows RsbU
508 concentrations to 10 μM. Below is the reaction scheme of RsbT binding to RsbU with the values
509 for the calculated $K_D$ below. **B** The rate of dephosphorylation of RsbV-P is plotted as a function
510 of concentration of $MnCl_2$ for RsbU (black) and $RsbU^{Q94L}$ (green) in the presence (dark) and
511 absence (light) of RsbT.. Curves are fits to the Michaelis-Menten equation using non-linear
512 curve fitting. The $k_{cat}$ of wild-type RsbU is 15 ± 0.35 $min^{-1}$ with RsbT and 1.4 ± 0.077 $min^{-1}$
513 without RsbT and the $k_{cat}$ of $RsbU^{Q94L}$ is 9.0 ± 0.64 $min^{-1}$ with RsbT and 2.4 ± 0.084 $min^{-1}$
514 without RsbT. The $K_M^{MnCl2}$ of wild-type RsbU is 0.98 ± 0.069 mM with RsbT and 77 ± 9.0 mM
515 without RsbT and the $K_M^{MnCl2}$ of $RsbU^{Q94L}$ is 1.4 ± 0.19 mM with RsbT and 1.9 ± 0.56 mM
516 without RsbT. The lower plot shows wild-type RsbU in the absence of RsbT for $MnCl_2$
517 concentrations to 100 mM. Below is a summary of a reaction scheme of RsbU
518 dephosphorylating RsbV-P (denoted as S) with the $K_M^{MnCl2}$ and $k_{cat}$ values below. Data for RsbU
519 are reproduced from (Ho & Bradshaw 2021). **C** A cartoon model of how the switch helices rotate
520 to activate RsbU. Binding of RsbT or mutation moves the switch helices into place during
521 activation to coordinate metal M2. The residues of RsbU that are hypothesized to coordinate
522 metals are shown as sticks (based on homology to RsbX).
523
524 **Figure 3: RsbT has a hybrid interface with RsbU N-terminal dimerization domain and**
525 **linker**
526 **A** An AlphaFold2 model of a heterotetrameric 2RsbT/2RsbU complex is shown in ribbon
527 representation. RsbT (purple) binds with an interface that spans the N-terminal domains (blue)

and α-helical linkers (grey) of both RsbU protomers. The PPM phosphatase domains are colored grey and the regulatory switch elements (α1 and α2) are colored orange. The Cα positions of $RsbU^{Y28}$ (red), *rsbU*$^{Y28I}$ suppressor substitutions (green), $RsbU^{R91}$ (dark pink), and $RsbT^{D92}$ (pink) are shown as spheres with the residue numbers indicated. **B** Strains with a $\sigma^B$ LacZ reporter were plated on IPTG/X-gal plates to induce expression of plasmid borne *rsbT* and *rsbU*$^{Y28I}$ and visualize $\sigma^B$ activity (indicated by blue pigmentation after 24 hours of growth at 37ºC). Additional amino acid substitutions in the *rsbU* gene are indicated above. **C** Strains with indicated changes to the RsbT and RsbU amino acid sequence were plated as in **B** and plates were imaged after 36 hours of growth at 37ºC. **D** R91E does not decrease the basal phosphatase activity of RsbU. Plots show dephosphorylation of RsbV-P (25 μM) by RsbU (black) and $RsbU^{R91E}$ (pink) (0.5μM) in the presence of 10 mM $MnCl_2$ and the presence or absence of 10 μM RsbT (light colors). Linear fits of the data are shown, with the slopes indicating the observed rates ($k_{obs}$): RsbU 0.0206 ± 0.00124 $min^{-1}$, RsbU + RsbT 10.0 ± 0.628 $min^{-1}$, $RsbU^{R91E}$ is 0.0379 ± 0.00543 $min^{-1}$, $RsbU^{R91E}$ + RsbT 0.142 ± 0.0161 $min^{-1}$. The lower plot is RsbU in the presence of RsbT to thirty minutes.

**Figure 4: RsbU linker is flexible in the absence of RsbT, and is rigidified by RsbT binding.** **A** I(q) versus q plot of the dimer component of SAXS scattering data from RsbU (blue) overlaid with a FoXS generated profile fit of the AlphaFold2 RsbU dimer structure (red). The lower plot shows the uncertainty normalized residuals of the fit ((experimental-computed)/error), $\chi^2$ of 12.53. **B** Dimensionless Kratky plot of SAXS scattering data from the dimer component of RsbU experimental data (blue). The experimental profile was logarithmically binned to reduce noise at high $qR_g$. **C** Normalized P(r) plot from the RsbU dimer (blue) and heterotetrameric

551 RsbT/RsbU$^{Q94L}$ complex (light blue) is shown. **D** I(q) versus q plot of the dimer component of
552 SAXS scattering data from RsbU (blue) is shown overlaid with a MultiFoXS generated two-state
553 profile fit with flexibility allowed for residues 82-96 (pink). The lower plot shows the
554 uncertainty normalized residuals of the fit ((experimental-computed)/error), $\chi^2$ of 1.2. **E**
555 Dimensionless Kratky plot of the heterotetrameric component of RsbT/RsbU$^{Q94L}$ complex is
556 shown binned logarithmically to reduce noise at high $qR_g$ values. **F** I(q) versus q plot of the
557 heterotetrameric RsbT/RsbU$^{Q94L}$ complex (blue) overlaid with a FoXS generated profile fit of the
558 AlphaFold2 RsbT/RsbU heterotetramer structure (red). The lower plot shows the uncertainty
559 normalized residuals of the fits ((experimental-computed)/error), $\chi^2$ of 1.83. **G** Schematic of the
560 conformational change of RsbU upon RsbT binding. The two best fit flexible models of RsbU
561 generated from MultiFoXS in panel **B** are shown with the calculated $R_g$ and percentage of each
562 model used in the fit.
563
564 **Figure 5: An exchangeable toolkit for bacterial signal transduction**
565 **A** An AlphaFold2 model of the *B. subtilis* energy stress phosphatase RsbP is shown bound to its
566 activating α/β-hydrolase protein RsbQ (purple) with a schematic of the $\sigma^B$ activation pathway
567 shown above. RsbP has an N-terminal PAS domain (turquoise) that is connected to the PPM
568 phosphatase domain by a predicted coiled coil linker. The Cα positions of bypass suppressor
569 mutations that render RsbP active in the absence of RsbQ (Brody et al. 2009) are shown as green
570 spheres. The switch element of the PPM phosphatase domain (α1 and α2) is colored orange. **B**
571 An AlphaFold2 model of the *C. difficile* GSR phosphatase RsbZ is shown with a schematic of
572 the $\sigma^B$ activation pathway shown above. RsbZ has tandem N-terminal GAF domains (blue) that
573 connect to the PPM phosphatase domain by a predicted coiled coil linker. The switch element of

the PPM phosphatase domain (α1 and α2) is colored orange. **C** Experimental structures of the GSR initiating adaptor protein RssB from *E. coli* (left, 8T85) and *P. aeruginosa* (right, 3F7A) are shown with a schematic of the $\sigma^S$ activation pathway shown above. The Cα positions of a bypass suppressor mutation (W143R) that renders RssB insensitive to anti-adapter proteins is shown as a green sphere. The switch element of the PPM phosphatase domain (α1 and α2) is colored orange. The black outline shows the portion of the PPM phosphatase domain that is missing in the *E. coli* RssB adaptor protein, which lacks phosphatase activity. **D** A cartoon schematic of activation by RsbT of proteins with RsbU NTD through ordering of a flexible linker. The protein is depicted with dimerized RsbU N-terminal dimerization domains (blue) with flexible linkers (black) that extend into two effector domains (grey). During stress conditions, RsbT (purple) activates the protein through binding to the N-terminal dimerization domains and linkers, rigidifying the linkers to dimerize the effector domains. **E** An AlphaFold2 model of a dimer of the histidine kinase NreB from a *Gammaproteobacteria* species (MBI3545564.1) is shown with the RsbU N-terminal domain colored blue and the histidine kinase domain colored pink. **F** An AlphaFold2 model of a dimer of the GGDEF diguanylate cyclase MtG from *M. thermoacetica* (WP_011392981.1) is shown with RsbU N-terminal domain colored blue, GAF domain colored lite blue, and GGDEF domain colored green. **G** Schematic illustrating how various sensor domains (RsbU N-terminal dimerization domain, PAS, response receiver (RR), and GAF) can control various output activities (serine/threonine phosphatase (PPM), histidine kinase (HK), protease adaptor, and diguanylate cyclase (GGDEF). We hypothesize that the shared regulatory mechanism through a dimeric coiled-coil linker makes these regulatory domains modularly exchangeable across effector domains. Known mechanisms

for how allosteric regulation is transmitted through the linker are listed and shown with arrow diagrams.

**Figure 1 – Figure Supplement 1: PAE plots of AlphaFold2 structure predictions**

Predicted aligned error of the AlphaFold2 structure predictions of the following proteins: *B. subtilis* RsbU, *B. subtilis* 2RsbT (chains A, B)/2RsbU (chains C,D) complex, *B. subtilis* 2RsbP (chains A,B)/2RsbQ complex (chains C,D), *C. difficile* RsbZ, *Gammaproteobacteria* sp. NreB, *M. thermoacetica* MtG, *M. tuberculosis* Rv1364c, *S. coelicolor* OsaC, *R. aetherivorans* WP_029544106.1, *S. coelicolor* MYU40396.1, and *Synechocystis* sp. WP_010874143.1. Blue indicates high confidence (0 Å) and red indicates low confidence (30 Å).

**Figure 1 – Figure Supplement 2: AlphaFold2 structure predictions with mapped pLDDT scores**

Predicted local distance difference test scores (pLDDT) mapped onto the AlphaFold2 structure predictions of the following proteins: *B. subtilis* RsbU, *B. subtilis* 2RsbT/2RsbU complex, *B. subtilis* 2RsbP/2RsbQ complex, *C. difficile* RsbZ, *Gammaproteobacteria* sp. NreB, *M. thermoacetica* MtG, *M. tuberculosis* Rv1364c, *S. coelicolor* OsaC, *R. aetherivorans* WP_029544106.1, *S. coelicolor* MYU40396.1, and *Synechocystis* sp. WP_010874143.1. The score key is above each structure model. Blue corresponds to a pLDDT score of 90-100 (high confidence), orange to yellow corresponds to a pLDDT score of 50-70 (medium confidence), and red corresponds to a pLDDT score of 0 (low confidence).

**Figure 1 – Figure Supplement 3: Q94L stabilizes the packing interface of the coiled-coil of the linker**

**A** Coil diagram of RsbU residues 83-97 generated using DrawCoil. Grey circles indicate non-polar residues, orange indicate polar residues, red indicate negatively charged residues, and blue indicate positively charged residues. The blue dashed line depicts a putative salt bridge. Residue Q94 (circled in green) sits in the interface of the coils and is shown packing with L90. **B** An allelic series of amino acid substitutions at position 94 of RsbU was generated in an *rsbU* expression plasmid. Plasmids were introduced into *B. subtilis* cells containing a LacZ reporter of $\sigma^B$ activity that were deleted for *rsbT* (top) or with *rsbT* retained on the chromosome (bottom). Cells were plated on IPTG/X-gal plates to induce *rsbU* expression and to indicate $\sigma^B$ activity (blue pigmentation). **C** α-helical pitch analysis of coiled-coil domains. The AlphaFold2 model of an RsbU dimer is overlayed with crystal structure of *P. aeruginosa* RssB (PDB 3F7A, purple, left). The helical linker region extending out of the coiled coil ($RsbU^{98-112}$) is shown (grey) overlaid with *T. maritima* transducing histidine kinase CheA (PDB 1B3Q, red, middle) and *Idiomarina* A28L diguanylyl cyclases PadC (PDB 5LLW, yellow, right). α angles from Crick parameterization analysis using CCCP are shown for the overlaid region.

**Figure 3 – Figure Supplement 1: RsbT binds to the linker**

Interface of RsbT and N-terminal domain of RsbU. A ribbon representation is shown of the AlphaFold2 model of the heterotetrameric 2RsbT/2RsbU complex with RsbU N-terminal dimerization domain colored blue, the switch element of the PPM domain (α1 and α2) colored orange, and RsbT colored purple. The Cα of positions of amino acids implicated in the binding interface of RsbT and RsbU N-terminal dimerization domain (Hardwick et al. 2007) are

641 represented on the AlphaFold2 structure as yellow spheres (RsbU) and green spheres (RsbT)
642 with the residue numbers.
643
644 **Figure 4 - Figure Supplement 1: MALS estimate of molecular weight of RsbU dimer,**
645 **RsbT/RsbU$^{Q94L}$ complex, RsbT/RsbU complex, and RsbU$^{Q94L}$**
646 **A** Plot of inline SEC-MALS analysis of RsbU with measured differential refractive index (blue,
647 left axis) and the molecular weight calculated from MALS (red, right axis). **B** Denaturing SDS-
648 PAGE gel of successive fractions from the equivalent range of the elution as shown in **A** from
649 preparative size exclusion chromatography of the sample of RsbU used for SEC-MALS-SAXS.
650 Black box denotes the C-terminal truncation product present in each lane of the main peak. **C**
651 Plots from inline SEC-MALS analysis of RsbT/RsbU$^{Q94L}$ complex with measured differential
652 refractive index (blue, left axis) and the molecular weight calculated from MALS (red, right
653 axis). **D** Denaturing SDS-PAGE gel of successive fractions from the equivalent range of the
654 elution of RsbT/U$^{Q94L}$ as shown in **C** from preparative size exclusion chromatography of the
655 sample used for SEC-MALS-SAXS. Black box denotes lack of C-terminal truncation product
656 during co-expression and purification of RsbT/RsbU$^{Q94L}$ complex. * Denotes load samples on
657 gel. **E** Plots from inline SEC-MALS analysis of RsbT/U complex with measured differential
658 refractive index (blue, left axis) and the molecular weight calculated from MALS (red, right
659 axis). **F** Plot inline SEC-MALS analysis of RsbU$^{Q94L}$ with measured differential refractive index
660 (blue, left axis) and the molecular weight calculated from MALS (red, right axis).
661
662 **Figure 4 – Figure Supplement 2: EFA deconvolution and Guinier analysis of RsbU dimer**
663 **SAXS profiles**

664 **A** SAXS data summary for RsbU. Series intensity (blue, left axis) versus frames, and $R_g$ versus
665 frame (red, right axis) are plotted. **B** The selected intensity range for EFA (black) (frame index
666 1330-1620), and the individual component ranges for deconvolution; blue denotes the range of
667 frames where the scattering component we assigned as the c0, RsbU dimer, was detected (frame
668 index 1330-1603) and orange denotes the range of frames where the scattering component that is
669 c1, presumably from a RsbU heterodimer containing a c-terminal truncation product dimer
670 (frame index 1357-1620). **C** Area normalized concentration profiles for the c0, RsbU dimer
671 component (blue) and c1, RsbU heterodimer containing c-terminal truncation product dimer
672 (orange). **D** Mean $\chi^2$ values for the fit of the EFA deconvolution to the original scattering data. **E**
673 Guinier fit for RsbU dimer component on the upper plot and uncertainty normalized residuals of
674 the fit on the lower plot. The scattering data for the dimer component (red) is fit to the Guinier
675 approximation (blue). The blue dashed lines are the $q_{min}$ and $q_{max}$ at values 0.00356 $Å^{-1}$ and
676 0.0234 $Å^{-1}$, respectively. **F** Kratky plot of SAXS scattering data from the dimer component of
677 RsbU experimental data (blue) overlaid with the profile computed by FoXS based on the
678 AlphaFold2 model of an RsbU dimer (red) and the profile of the flexible model computed by
679 MultiFoXS (pink). The experimental profile was logarithmically binned to reduce noise at high
680 q.
681
682 **Figure 4 – Figure Supplement 3: Varying constraints and flexibility of RsbU model**
683 **A** I(q) versus q plot of the dimer component of SAXS scattering data from RsbU (blue) overlaid
684 with a MultiFoXS generated two-state profile fit with flexibility allowed for residues 82-86
685 (pink). The upper plot shows I(q) versus q on log-linear axes while the lower plot shows the
686 uncertainty normalized residuals of the fit ((experimental-computed)/error), $\chi^2$ of 1.26. **B** I(q)

687 versus q plot of the dimer component of SAXS scattering data from RsbU (blue) overlaid with a
688 MultiFoXS generated two-state profile fit with flexibility allowed for residues 82-92 (pink). The
689 upper plot shows I(q) versus q on log-linear axes while the lower plot shows the uncertainty
690 normalized residuals of the fit ((experimental-computed)/error), $\chi^2$ of 1.25. **C** I(q) versus q plot
691 of the dimer component of SAXS scattering data from RsbU (blue) overlaid with a MultiFoXS
692 generated two-state profile fit with flexibility allowed for residues 92-99 (pink). The upper plot
693 shows I(q) versus q on log-linear axes while the lower plot shows the uncertainty normalized
694 residuals of the fit ((experimental-computed)/error), $\chi^2$ of 1.26. **D** I(q) versus q plot of the dimer
695 component of SAXS scattering data from RsbU (blue) overlaid with a MultiFoXS generated
696 two-state profile fit with flexibility allowed for residues 82-96 (pink) and the C-terminal domains
697 constrained. The upper plot shows I(q) versus q on log-linear axes while the lower plot shows the
698 uncertainty normalized residuals of the fit ((experimental-computed)/error), $\chi^2$ of 5.4.
699

700 **Figure 4 – Figure Supplement 4: EFA deconvolution and Guinier analysis of**
701 **RsbT/RsbU$^{Q94L}$ SAXS profiles**

702 **A** SAXS data summary for RsbT/RsbU$^{Q94L}$. Series intensity (blue, left axis) versus frames, and
703 $R_g$ versus frame (red, right axis) are plotted. **B** The selected intensity range for EFA (black)
704 (frame index 1300-1540), and the individual component ranges for deconvolution; blue denotes
705 the range of frames where the scattering component we assigned as c0, ambiguous component,
706 was detected (1300-1461) and orange denotes the range of frames where the scattering
707 component we assigned as c1, the 2RsbT/2RsbU$^{Q94L}$ heterotetrametric complex, was detected
708 (1318-1540). **C** Area normalized concentration profiles for 2RsbT/2RsbU$^{Q94L}$ heterotetrameric
709 complex (orange) and ambiguous component (blue). **D** Mean $\chi^2$ values for the EFA

deconvolution fit to the original scattering data. **E** Guinier fit for 2RsbT/2RsbU$^{Q94L}$ heterotetrameric complex component on the upper plot and uncertainty normalized residuals of the fit on the lower plot. The scattering data for the dimer component (red) is fit to the Guinier approximation (blue). The blue dashed lines are the $q_{min}$ and $q_{max}$ at values 0.0033 Å$^{-1}$ and 0.0336 Å$^{-1}$, respectively. **F** I(q) versus q plot of the heterotetrameric complex component of SAXS scattering data from 2RsbT/2RsbU (blue) overlaid with a MultiFoXS generated two-state profile fit with flexibility allowed for residues 82-96 (red). The upper plot shows I(q) versus q on log-linear axes while the lower plot shows the uncertainty normalized residuals of the fit ((experimental-computed)/error), $\chi^2$ of 1.96. The one-state flexible model is shown with a RMSD to the AlphaFold2 prediction of 2RsbT/2RsbU of 1.36 Å. **G** Kratky plot of SAXS scattering data from the heterotetrameric component of 2RsbT/2RsbU experimental data (blue) overlaid with the profile computed by FoXS based on the AlphaFold2 model of an RsbT/RsbU heterotetramer (red). The experimental profile was logarithmically binned to reduce noise at high q.

**Figure 5 – Figure Supplement 1: AlphaFold2 predictions of varying signaling PPM phosphatases**

**A** An AlphaFold2 model of the *M. tubercolisis* GSR phosphatase Rv1364c is shown with a N-terminal PAS domain colored turquoise that connects to the PPM phosphatase domain colored grey, an anti-σ domain (related to RsbW) colored pink and an anti-anti-σ domain (related to RsbV) colored purple. The switch element of the PPM phosphatase domain (α1 and α2) is colored orange. **B** An AlphaFold2 model of the *S. coelicolor* OsaC GSR phosphatase is shown with a N-terminal RsbW-like kinase domain colored in green, connected to a PAS domain colored in turquoise, tandem GAF domains colored in blue, and a PPM phosphatase colored in

grey. The switch element of the PPM phosphatase domain (α1 and α2) is colored orange. **C** An AlphaFold2 model of a dimer of the phosphatase from *R. aetherivorans* (WP_029544106.1) is shown with the GAF domain colored in blue connected to the PPM phosphatase colored in grey. The switch element of the PPM phosphatase domain (α1 and α2) is colored orange. **D** An AlphaFold2 model of a dimer of the phosphatase from *S. coelicolor* (MYU40396.1) is shown with the response receiver domain colored in red connected to the PPM phosphatase colored in grey. The switch element of the PPM phosphatase domain (α1 and α2) is colored orange. **E** An AlphaFold2 model of a dimer of the phosphatase from *Synechocystis* species (WP_010874143.1) is shown with the HAMP domain colored in yellow connected to the PPM phosphatase colored in grey. The switch element of the PPM phosphatase domain (α1 and α2) is colored orange. The structure models in all panels are shown aligned by the top PPM domain to highlight the conservation of the PPM dimer in predictions of dimeric phosphatases with diverse regulatory domains.

**Figure 5 – Figure Supplement 2: Coiled-coil analysis of structures of bacterial signaling enzymes**

Models of selected phosphatases are shown (**A,** heterotetramer of RsbPQ from *B. subtilis*; **B,** RsbZ from *C. difficile*; **C**, RssB from *P. aeruginosa* (PDB: 3EQ2); **D**, NreB from *Gammaproteobacteria*; **E**, MtG from *M. thermoacetica*; **F**, Rv1364c from *M. tuberculosis*; **G**, OsaC from *S. coelicolor*; **H**, WP_029544106.1 from *R. aetherivorans*; **I,** MYU40396.1 from *S. coelicolor*; **J**, WP_010874143.1 from *Synechocystis sp.* Coiled-coil sequences identified by Socket2 are shown above the model with the non-polar positions of *a* and *d* shown in pink above the sequence. Polar residues at the *a* and *d* positions are in bold. The coiled-coil region on the

model is shown in pink, the switch helices of the PPM domains are shown in orange, and the various regulatory domains are shown in the following colors: RsbU NTD (blue), PAS (green), GAF (light blue), response receiver (red), and HAMP (yellow).

## Materials and Methods

### Protein expression and purification

All proteins were expressed in *E. coli* BL21 (DE3) cells grown at 37ºC to an $OD_{600}$ of 0.4 and induced at 16ºC for 14-18 hours with 1mM isopropyl β-d-1-thiogalactopyranoside (IPTG) unless otherwise specified. Cells were harvested and purified as follows:

*RsbU and RsbU variants*: Cell pellets were resuspended in lysis buffer with 1 mM phenylmethylsulfonyl fluoride (PMSF) (50 mM K•HEPES, pH 7.5, 100 mM NaCl, 20 mM imidazole, 10% glycerol, 0.5 mM dithiothreitol (DTT)), and were lysed using two passes in a microfluidizer at 10,000 PSI. Cell lysates were cleared by spinning at 16,000 RPM for 45 minutes in an Avanti JA-20 rotor. Cleared lysates were then run over a HisTrap HP column on an AKTA FPLC, washed with lysis buffer, and eluted with a gradient to 200 mM imidazole. RsbU was run on a Superdex200 16/600 column equilibrated with lysis buffer on an AKTA FPLC. Fractions were pooled and the 6-His tags were cleaved with 3C protease in dialysis to lysis buffer overnight at 4ºC. Cleaved tags and 3C protease were subtracted by passing over a column containing equilibrated Ni-NTA resin. 2 mM EDTA was added to cleaved protein prior to gel filtration run. RsbU was then further purified on a Superdex200 16/600 column

equilibrated with 20 mM K•HEPES pH 7.5, 100 mM NaCl, 2 mM DTT on an AKTA FPLC. Fractions were pooled, concentrated to 200 μM, and flash-frozen and stored at -80ºC.

*RsbT/U and RsbT/RsbU$^{Q94L}$ co-expression*: Cell pellets were resuspended in lysis buffer with 1 mM PMSF (50 mM K•HEPES pH 8.0, 200 mM NaCl, 20 mM imidazole, 10% glycerol, 0.5 mM DTT), and were lysed using two passes in a microfluidizer at 10,000 PSI. Cell lysates were cleared by spinning at 16,000 RPM for 45 minutes in an Avanti JA-20 rotor. Cleared lysates were then run over a HisTrap HP column on an AKTA FPLC, washed with lysis buffer, and eluted with a gradient to 200 mM imidazole. 2 mM EDTA was added to protein prior to gel filtration run. RsbT/RsbU was then further purified on a Superdex200 16/600 column equilibrated with 20 mM K•HEPES pH 8.0, 100 mM NaCl, 2 mM DTT on an AKTA FPLC. Fractions were pooled, concentrated to 200 μM, and flash-frozen and stored at -80ºC.

*RsbT*: Cells were resuspended in lysis buffer with 1 mM PMSF (50 mM K•HEPES pH 8.0, 100 mM NaCl, 20 mM imidazole, 10% glycerol, 2 mM $MgCl_2$, 0.1 mM ATP, 0.5 mM DTT), and were lysed using two passes in a microfluidizer at 10,000 PSI. Cell lysates were cleared by spinning at 16,000 RPM for 45 minutes in an Avanti JA-20 rotor. Cleared lysates were then run over 2 mL/L of cells of Ni-NTA resin slurry equilibrated with lysis buffer. The resin was then washed with 10 CV of lysis buffer. Ni-NTA resin was resuspended with 10 mL of lysis buffer with 400 mM imidazole, and was incubated for 10 minutes. RsbT was eluted off column, elution was tracked by Bradford Reagent. Additional elution buffer was added until all protein was eluted off column. The 6-His tags were cleaved with 3C protease in dialysis to lysis buffer overnight at 4ºC. Cleaved tags and 3C protease were subtracted by passing over a column

801 containing equilibrated Ni-NTA resin. Protein was concentrated to approximately 50 uM, was
802 flash-frozen and stored at -80ºC.
803
804 *RsbV:* RsbV was expressed in *E. coli* BL21 (DE3) cells grown at 37ºC to an $OD_{600}$ of 0.4 and
805 induced at 37ºC for 3-4 hours with 1mM IPTG. Cells were harvested and resuspended in lysis
806 buffer with 1 mM PMSF (50 mM K•HEPES pH 8.0, 200 mM NaCl, 20 mM imidazole, 10%
807 glycerol, 0.5 mM DTT), and were lysed using two passes on a microfluidizer at 10,000 PSI. Cell
808 lysates were cleared by spinning at 16,000 RPM for 45 minutes in an Avanti JA-20 rotor.
809 Cleared lysates were then run over a HisTrap HP column on an AKTA FPLC, washed with lysis
810 buffer, and eluted with a gradient to 200 mM imidazole. 2 mM EDTA was added to protein prior
811 to gel filtration run. The 6-His tags were cleaved with 3C protease in dialysis to lysis buffer
812 overnight at 4ºC. Cleaved tags and 3C protease were subtracted by passing over a column
813 containing equilibrated Ni-NTA resin. Cleaved protein was then further purified on a
814 Superdex75 16/60 equilibrated in 20 mM K•HEPES pH 7.5, 150 mM NaCl, 10 % glycerol, 2
815 mM DTT. Fractions were pooled, concentrated to approximately 100 µM, and flash-frozen and
816 stored at -80ºC.
817
818 *RsbW*: Cell pellets were resuspended in lysis buffer with 1 mM PMSF (20 mM K•HEPES pH
819 7.5, 200 mM NaCl, 20 mM imidazole, 10 mM $MgCl_2$, 10 % glycerol, and 0.5 mM DTT), and
820 were lysed using two passes on a microfluidizer at 10,000 PSI. Cell lysates were cleared by
821 spinning at 16,000 RPM for 45 minutes in an Avanti JA-20 rotor. Cleared lysates were then run
822 over a HisTrap HP column on an AKTA FPLC, washed with lysis buffer, and eluted with a
823 gradient to 200 mM imidazole. The 6H tag was left uncleaved to aid removal after

824 phosphorylation reactions. RsbW was then further purified on a Superdex75 16/60 equilibrated
825 in 50 mM K•HEPES pH 7.5, 150 mM NaCl, 10% glycerol, and 2 mM DTT. Fractions were
826 pooled, concentrated to approximately 100 µM, and flash-frozen and stored at -80ºC.
827
828 *RsbV-P:* RsbVW coexpression plasmid was expressed in *E. coli* BL21 (DE3) cells grown at 37ºC
829 to an $OD_{600}$ of 0.4 and induced at 37ºC for 3-4 hours with 1mM IPTG. Cells were harvested and
830 resuspended in lysis buffer with 1 mM PMSF (50 mM K•HEPES pH 7.5, 50 mM KCl, 20 mM
831 imidazole, 0.5 mM DTT), and were lysed using two passes on a microfluidizer at 10,000 PSI.
832 Cell lysates were cleared by spinning at 16,000 RPM for 45 minutes in an Avanti JA-20 rotor.
833 Cleared lysates were then run over a HisTrap HP column on an AKTA FPLC, washed with lysis
834 buffer, and eluted with a gradient to 200 mM imidazole. The 6-His tags were cleaved with 3C
835 protease in dialysis to lysis buffer overnight at 4ºC. Cleaved tags and 3C protease were
836 subtracted by passing over a column containing equilibrated Ni-NTA resin. RsbVW was run on a
837 Superdex75 16/60 column equilibrated with lysis buffer on an AKTA FPLC. Fractions of
838 RsbVW coelution were pooled and RsbV was phosphorylated in dialysis at room temperature in
839 lysis buffer with 5 mM ATP and 10 mM $MgCl_2$. RsbV-P Fractions were pooled, concentrated to
840 200 µM, and flash-frozen and stored at -80ºC. Dialyzed RsbVW were then concentrated and run
841 on Superdex75 16/60 column equilibrated with 20 mM K•HEPES pH 7.5, 150 mM NaCl, 10%
842 glycerol, 2 mM DTT. RsbV-P Fractions were pooled, concentrated to 200 µM, and flash-frozen
843 and stored at -80ºC.
844
845 **SEC-MALS-SAXS**

846 Small Angle X-ray Scattering (SAXS) was performed at BioCAT (beamline 18ID at the
847 Advanced Photon Source, Chicago) with in-line size exclusion chromatography (SEC) to
848 separate sample from aggregates and other contaminants and ensure optimal sample quality. In-
849 line multiangle light scattering (MALS), dynamic light scattering (DLS) and differential
850 refractive index (dRI) measurements were recorded for additional biophysical characterization
851 (SEC-MALS-SAXS). The samples were loaded on a Superdex 200 10/300 Increase GL Column
852 (Cytiva) run by a 1260 Infinity II HPLC (Agilent Technologies) at 0.6 ml/min. The flow passed
853 in order through an Agilent UV detector, a MALS detector and a DLS detector (DAWN Helios
854 II, Wyatt Technologies), and an RI detector (Optilab T-rEX, Wyatt) before the SAXS flow cell.
855 The flow cell consists of a 1.0 mm ID quartz capillary with ~20 µm walls. A coflowing buffer
856 sheath is used to separate sample from the capillary walls, helping prevent radiation damage
857 (Kirby et al. 2016) . Scattering intensity was recorded using a Pilatus3 X 1M (Dectris) detector
858 that was placed 3.682 m from the sample giving us access to a q-range of 0.0027 $Å^{-1}$ to 0.33 $Å^{-1}$.
859 0.5s exposures were acquired every 1 s during elution and data was reduced using BioXTAS
860 RAW 2.1.4 (Hopkins et al. 2017) (Hopkins 2024). Buffer blanks were created by averaging
861 regions flanking the elution peak and subtracted from all measured profiles. Because of the
862 heterogeneity in the samples, evolving factor analysis (EFA) was used to deconvolve the
863 scattering profiles of the overlapping components (Meisburger et al. 2016). These scattering
864 profiles were used for subsequent analysis in RAW. The quality of the deconvolution was
865 assessed based on the mean weighted $\chi^2$ for each deconvoluted component and the $\chi^2$ of the
866 combined fit to each frame of the dataset (Figure 4 – Figure Supplement 2B-E, Figure 4 – Figure
867 Supplement 4B-E). RAW was used to run GNOM from the ATSAS package (version 3.2.1)
868 (Svergun 1992; Manalastas-Cantos et al. 2021). Description of each SAXS sample and results of

869 the analysis are presented in Table 1 (Trewhella et al. 2017).The composition of each scattering
870 component was determined based on the SAXS derived molecular weights, the MALS profile,
871 and gels from the purification of the protein or protein complex (Figure 4 – Figure Supplement 1;
872 Table 1). Molecular weights and hydrodynamic radii were calculated from the MALS and DLS
873 data respectively using the ASTRA 7 software (Wyatt). All samples were run in 20 mM HEPES
874 pH 7.5, 100 mM NaCl, 5 mM DTT. Wild-type RsbU was run at a concentration of 3.5 mg/mL,
875 RsbT/RsbU$^{Q94L}$ was run at a concentration of 2.5 mg/mL, RsbU$^{Q94L}$ was run at a concentration of
876 3.5 mg/mL, RsbT/RsbU was run at a concentration of 2.5 mg/mL. FoXS was used to calculated
877 predicted scattering profiles from the model, and was compared to the experimental scattering
878 profiles (Schneidman-Duhovny et al. 2016; Schneidman-Duhovny et al. 2013). Output
879 parameters calculated using FoXS are provided in Table 1. MultiFoXS was used to generate a
880 flexible structure ensemble with multicomponent fits and was compared to the experimental
881 scattering profiles (Schneidman-Duhovny et al. 2016). MultiFoXS input and output parameters
882 are provided in Table 1.
883
884 **Fluorescence anisotropy**
885 We site-specifically labeled RsbT with tetramethylrhodamine 5-maleimide (TMR) dye at its
886 unique cysteine (position 6). We added increasing concentrations of RsbU and RsbU$^{Q94L}$ to
887 200nM RsbT$^{TMR}$ and measured the change in anisotropy (Figure 2A). All measurements were
888 done at 25ºC in 50 mM K•HEPES pH 7.5, 100 mM NaCl, and 10% glycerol. All measurements
889 of spectra were conducted with a slit width of 7 nm, and anisotropy measurements were
890 conducted with a slit width of 7 nm. The excitation wavelength was 551 nm and the emission
891 wavelength was 577 nm. Anisotropy measurements were taken 30 seconds apart for 6

892 measurements, and then were averaged and plot against its corresponding concentration of RsbU.
893 Anisotropy data was then fit to a quadratic binding curve using KaleidaGraph, reported errors are
894 the error of the fit.
895
896 **Phosphatase assays**
897 Phosphatase assays were performed with RsbV-P that was labeled with $^{32}P$ by incubating RsbV
898 (40 μM), 6His-RsbW (45 μM), and 100 μCi of γ-$^{32}P$ ATP overnight at room temperature in 50
899 mM K•HEPES pH 7.5, 50 mM KCl, 10 mM $MgCl_2$, and 2 mM DTT. Unincorporated nucleotide
900 was removed by buffer exchange using a Zeba spin column equilibrated in 50 mM K•HEPES pH
901 8.0, 100 mM NaCl. 6H-RsbW was then removed by Ni-NTA resin equilibrated in 50 mM
902 K•HEPES pH 8.0, 100 mM NaCl, 20 mM imidazole. The flow-through fraction from the Ni-
903 NTA resin containing RsbV-$^{32}P$ was then exchanged into 50 mM K•HEPES pH 8.0, 100 mM
904 NaCl buffer using 3 subsequent Zeba spin columns to remove all unincorporated nucleotide and
905 free phosphate. Labeled RsbV-$^{32}P$ was aliquoted and frozen at -80ºC for future use.
906
907 All phosphatase assays were performed at room temperature in 50 mM K•HEPES pH 7.5, 100
908 mM NaCl. The concentrations of enzyme, substrate, $MnCl_2$, and $MgCl_2$ were varied as indicated.
909 10 μM RsbT was additionally added to reactions as indicated. Reactions were stopped with 0.5
910 M EDTA, pH 8.0 and run on PEI-Cellulose TLC plates developed in 1 M $LiCl_2$ and 0.8 M acetic
911 acid and imaged on a Typhoon scanner. Phosphatase assays were performed more than three
912 independent times as separate experiments. Data shown in figures is from a single representative
913 experiment, and reported errors are the error from the fit.
914

915 ***B. subtilis* strain construction**

916 *B. subtilis* cells were grown in Lennox lysogeny broth (LB, Sigma Aldrich) as liquid medium or
917 as plates supplemented with 15% Bacto Agar (Difco). Antibiotics were used as appropriate for
918 maintenance of plasmids or for selection of transformants: MLS (50 µg/ml erythromycin, 250
919 µg/ml lincomycin), kanamycin (10 µg/ml). For plates used to visualize $\sigma^B$ reporter activity, 80
920 µg/ml of 5-bromo-4-chloro-3-indolyl-β-D-galactopyranoside (X-gal) and 1 mM IPTG were
921 added. All *B. subtilis* strains were derived from the PY79 strain background and are listed in the
922 table of strains. Plasmids based on pHB201(Bron et al. 1998) were introduced to *B. subtilis*
923 strains using natural competence(Harwood & Cutting 1990).

924

925 **Genetic screens**

926 Genetic screens were performed as described previously (Ho & Bradshaw 2021). Plasmids
927 containing *rsbU* or *rsbT/rsbU*$^{Y28I}$ were subjected to PCR mutagenesis using GoTaq DNA
928 polymerase mix (Promega) supplemented with 2mM additional $MgCl_2$. Pools of mutagenized
929 inserts were assembled into digested plasmid using isothermal (Gibson) assembly and
930 transformed into *E. coli* DH5α cells. Mutation rate of approximately one single-nucleotide
931 polymorphism per kilobase of DNA was confirmed by sequencing individual clones. Plasmids
932 were then introduced to *B. subtilis* using natural competence and cells were plated on selective
933 medium containing IPTG and X-gal for two days at 37ºC. Blue colonies were selected, restruck
934 on plates with and without IPTG, and plasmids recovered from single colonies that retested as $\sigma^B$
935 positive were sequenced using Sanger sequencing. For the RsbU$^{Y28I}$ suppressor screen, two
936 independent pools of PCR mutagenized plasmid were screened. In addition to the reported
937 variants that were selected, we identified simple revertants that restored Y28 in both pools, and

938 mutations in the promoter and RBS that we predict enhanced protein production. These variants
939 were not studied further. Individual amino acid changing mutations were rebuilt in the parental
940 plasmid using PCR (QuickChange) mutagenesis and the phenotypes were validated by replating
941 on indicator plates. All strains shown in the figures are from these rebuilt plasmids.
942
943 **AlphaFold2 structure predictions**
944 AlphaFold2 predictions were performed using ColabFold (Mirdita et al. 2022).
945 Alphafold2_multimer_v2 was used in unpaired_paired mode with no templates with 3 recycles,
946 200 iterations, and greedy pairing strategy. The predicted aligned error plots for all AlphaFold2
947 structures are shown in Figure 1 – Figure Supplement 1. The predicted local distance difference
948 test scores (pLDDT) mapped onto the structures are shown in Figure 1 – Figure Supplement 2.
949
950 **Socket2 analysis of AlphaFold2 structure predictions**
951 Socket2 coiled-coil predictions were performed using Socket2 Colab (Kumar & Woolfson 2021).
952 Socket2 was used with a packing cutoff of 7.0Å. Analysis done using Socket2 is shown in Figure
953 5 – Figure Supplement 2.
954

## References


Bartolini, M. et al., 2019. Regulation of Biofilm Aging and Dispersal in Bacillus subtilis by the Alternative Sigma Factor SigB. *Journal of Bacteriology*, 201(2).

Battesti, A. et al., 2013. Anti-adaptors provide multiple modes for regulation of the RssB adaptor protein. *Genes & development*, 27(24), pp.2722–2735.

Battesti, A., Majdalani, N. & Gottesman, S., 2015. Stress sigma factor RpoS degradation and translation are sensitive to the state of central metabolism. *Proceedings of the National Academy of Sciences of the United States of America*.

Battesti, A., Majdalani, N. & Gottesman, S., 2011. The RpoS-mediated general stress response in Escherichia coli. *Annual review of microbiology*, 65, pp.189–213.

Bergkessel, M., Basta, D.W. & Newman, D.K., 2016. The physiology of growth arrest: uniting molecular and environmental microbiology. *Nature Reviews Microbiology*, 14(9), pp.549–562.

Bilwes, A.M. et al., 1999. Structure of CheA, a signal-transducing histidine kinase. *Cell*, 96(1), pp.131–141.

Boekhoud, I.M. et al., 2020. Redefining the Clostridioides difficile σB Regulon: σB Activates Genes Involved in Detoxifying Radicals That Can Result from the Exposure to Antimicrobials and Hydrogen Peroxide. *mSphere*, 5(5).

Boylan, S.A., Redfield, A.R. & Price, C.W., 1993. Transcription factor sigma B of Bacillus subtilis controls a large stationary-phase regulon. *Journal of Bacteriology*, 175(13), pp.3957–3963.

Bradshaw, N. et al., 2017. A widespread family of serine/threonine protein phosphatases shares a common regulatory switch with proteasomal proteases. *eLife*, 6.

Brody, M.S., Stewart, V. & Price, C.W., 2009. Bypass suppression analysis maps the signalling pathway within a multidomain protein: the RsbP energy stress phosphatase 2C from Bacillus subtilis. *Molecular microbiology*, 72(5), pp.1221–1234.

Bron, S. et al., 1998. Protein secretion and possible roles for multiple signal peptidases for precursor processing in bacilli. *Journal of biotechnology*, 64(1), pp.3–13.

Brugger, C., Schwartz, J., et al., 2023. Structure of phosphorylated-like RssB, the adaptor delivering σs to the ClpXP proteolytic machinery, reveals an interface switch for activation. *The Journal of biological chemistry*, 299(12), p.105440.

Brugger, C., Srirangam, S. & Deaconescu, A.M., 2023. IraM Remodels the RssB Segmented Helical Linker to Stabilize σs Against Degradation by ClpXP. *The Journal of biological chemistry*, p.105568.

Chakravarty, D. & Porter, L.L., 2022. AlphaFold2 fails to predict protein fold switching. *Protein Science*, 31(6), p.e4353.

Cordeiro, T.N. et al., 2017. Structural Characterization of Highly Flexible Proteins by Small-Angle Scattering. *Advances in experimental medicine and biology*, 1009, pp.107–129.

de Been, M. et al., 2010. A novel hybrid kinase is essential for regulating the sigma(B)-mediated stress response of Bacillus cereus. *Environmental microbiology*, 12(3), pp.730–745.

Delumeau, O. et al., 2004. Functional and structural characterization of RsbU, a stress signaling protein phosphatase 2C. 279(39), pp.40927–40937.

Dorich, V. et al., 2019. Structural basis for inhibition of a response regulator of σS stability by a ClpXP antiadaptor. *Genes & development*, 33(11-12), pp.718–732.

Fernández Martínez, L. et al., 2009. Osmoregulation in Streptomyces coelicolor: modulation of SigB activity by OsaC. *Molecular microbiology*, 71(5), pp.1250–1262.

Galperin, M.Y., 2006. Structural classification of bacterial response regulators: diversity of output domains and domain combinations., 188(12), pp.4169–4182.

Gottesman, S., 2019. Trouble is coming: Signaling pathways that regulate general stress responses in bacteria.

Gourinchas, G. et al., 2017. Long-range allosteric signaling in red light-regulated diguanylyl cyclases. *Science advances*, 3(3), p.e1602498.

Greenstein, A.E. et al., 2009. Interdomain communication in the Mycobacterium tuberculosis environmental phosphatase Rv1364c., 284(43), pp.29828–29835.

Grigoryan, G. & DeGrado, W.F., 2011. Probing designability via a generalized model of helical bundle geometry., 405(4), pp.1079–1100.

Guerreiro, D.N., Arcari, T. & O'Byrne, C.P., 2020. The σB-Mediated General Stress Response of Listeria monocytogenes: Life and Death Decision Making in a Pathogen. *Frontiers in microbiology*, 11, p.1505.

Guldimann, C. et al., 2016. Resilience in the face of uncertainty: sigma B fine-tunes gene expression to support homeostasis in Gram-positive bacteria. *Applied and Environmental Microbiology*.

Haldenwang, W.G. & Losick, R., 1979. A modified RNA polymerase transcribes a cloned gene under sporulation control in Bacillus subtilis. *Nature*, 282(5736), pp.256–260.

Hardwick, S.W. et al., 2007. Structural and functional characterization of partner switching regulating the environmental stress response in Bacillus subtilis. 282(15), pp.11562–11572.

Harms, A., Maisonneuve, E. & Gerdes, K., 2016. Mechanisms of bacterial persistence during stress and antibiotic exposure. 354(6318), pp.aaf4268–aaf4268.

Harwood, C.R. & Cutting, S.M., 1990. Molecular Biological Methods for Bacillus. pp.1–308.

Hecker, M., Pané-Farré, J. & Völker, U., 2007. SigB-dependent general stress response in Bacillus subtilis and related gram-positive bacteria. *Annual review of microbiology*, 61, pp.215–236.

Heinz, V. et al., 2022. The Vibrio vulnificus stressosome is an oxygen-sensor involved in regulating iron metabolism. *Communications biology*, 5(1), p.622.

Herbert, S. et al., 2010. Repair of global regulators in Staphylococcus aureus 8325 and comparative analysis with other clinical isolates. *Infection and immunity*, 78(6), pp.2877–2889.

Ho, K. & Bradshaw, N., 2021. A conserved allosteric element controls specificity and activity of functionally divergent PP2C phosphatases from B. subtilis. *The Journal of biological chemistry*, p.100518.

Hopkins, J.B., Gillilan, R.E. & Skou, S., 2017. BioXTAS RAW: improvements to a free open-source program for small-angle X-ray scattering data reduction and analysis. *Journal of applied crystallography*, 50(Pt 5), pp.1545–1553.

Jumper, J. et al., 2021. Highly accurate protein structure prediction with AlphaFold. *Nature*, 596(7873), pp.583–589.

Kikhney, A.G. & Svergun, D.I., 2015. A practical guide to small angle X-ray scattering (SAXS) of flexible and intrinsically disordered proteins. *FEBS letters*, 589(19 Pt A), pp.2570–2577.

Kint, N. et al., 2017. The alternative sigma factor σ(B) plays a crucial role in adaptive strategies of Clostridium difficile during gut infection. *Environmental microbiology*.

Kint, N. et al., 2019. The σB signalling activation pathway in the enteropathogen Clostridioides difficile. *Environmental microbiology*, 21(8), pp.2852–2870.

Kirby, N. et al., 2016. Improved radiation dose efficiency in solution SAXS using a sheath flow sample environment. *Acta crystallographica. Section D, Structural biology*, 72(Pt 12), pp.1254–1266.

Kumar, P. & Woolfson, D.N., 2021. Socket2: a program for locating, visualizing and analyzing coiled-coil interfaces in protein structures. *Bioinformatics (Oxford, England)*, 37(23), pp.4575–4577.

Manalastas-Cantos, K. et al., 2021. ATSAS 3.0: expanded functionality and new tools for small-angle scattering data analysis. *Journal of applied crystallography*, 54(Pt 1), pp.343–355.

Marles-Wright, J. et al., 2008. Molecular architecture of the “stressosome,” a signal integration and transduction hub., 322(5898), pp.92–96.

Meisburger, S.P. et al., 2016. Domain Movements upon Activation of Phenylalanine Hydroxylase Characterized by Crystallography and Chromatography-Coupled Small-Angle X-ray Scattering. *Journal of the American Chemical Society*, 138(20), pp.6506–6516.

Mirdita, M. et al., 2022. ColabFold: making protein folding accessible to all. *Nature methods*, 19(6), pp.679–682.

Mittenhuber, G., 2002. A phylogenomic study of the general stress response sigma factor sigmaB of Bacillus subtilis and its regulatory proteins. *Journal of Molecular Microbiology and Biotechnology*, 4(4), pp.427–452.

Möglich, A., Ayers, R.A. & Moffat, K., 2009. Structure and signaling mechanism of Per-ARNT-Sim domains. *Structure (London, England : 1993)*, 17(10), pp.1282–1294.

Nadezhdin, E.V., Brody, M.S. & Price, C.W., 2011. An α/β Hydrolase and Associated Per-ARNT-Sim Domain Comprise a Bipartite Sensing Module Coupled with Diverse Output Domains. *PLoS ONE*, 6(9), p.e25418.

Quin, M.B. et al., 2012. The bacterial stressosome: a modular system that has been adapted to control secondary messenger signaling. *Structure (London, England : 1993)*, 20(2), pp.350–363.

Rambo, R.P. & Tainer, J.A., 2011. Characterizing flexible and intrinsically unstructured biological macromolecules by SAS using the Porod-Debye law. *Biopolymers*, 95(8), pp.559–571.

Randall, T.E. et al., 2022. Sensory Perception in Bacterial Cyclic Diguanylate Signal Transduction. *Journal of Bacteriology*, 204(2), p.e0043321.

Receveur-Bréchot, V. & Durand, D., 2012. How random are intrinsically disordered proteins? A small angle scattering perspective. *Current protein & peptide science*, 13(1), pp.55–75.

Rodríguez-Martínez, K. et al., 2023. Defining the regulatory mechanisms of sigma factor RpoS degradation in Azotobacter vinelandii and Pseudomonas aeruginosa. *Molecular microbiology*, 120(1), pp.91–102.

Schneidman-Duhovny, D. et al., 2013. Accurate SAXS profile computation and its assessment by contrast variation experiments. *Biophysical journal*, 105(4), pp.962–974.

Schneidman-Duhovny, D. et al., 2016. FoXS, FoXSDock and MultiFoXS: Single-state and multi-state structural modeling of proteins and their complexes based on SAXS profiles. *Nucleic Acids Research*, 44(W1), pp.W424–9.

Svergun, D.I., 1992. Determination of the regularization parameter in indirect-transform methods using perceptual criteria. *Journal of applied crystallography*, 25, pp.495–503.

Trewhella, J. et al., 2017. 2017 publication guidelines for structural modelling of small-angle scattering data from biomolecules in solution: an update. *Acta crystallographica. Section D, Structural biology*, 73(Pt 9), pp.710–728.

Tuchscherr, L. & Löffler, B., 2016. Staphylococcus aureus dynamically adapts global regulators and virulence factor expression in the course from acute to chronic infection. *Current genetics*, 62(1), pp.15–17.

Vijay, K. et al., 2000. A PP2C phosphatase containing a PAS domain is required to convey signals of energy stress to the sigmaB transcription factor of Bacillus subtilis. *Molecular microbiology*, 35(1), pp.180–188.

Yang, X. et al., 1996. Opposing pairs of serine protein kinases and phosphatases transmit signals of environmental stress to activate a bacterial transcription factor. *Genes & development*, 10(18), pp.2265–2275.

Zschiedrich, C.P., Keidel, V. & Szurmant, H., 2016. Molecular Mechanisms of Two-Component Signal Transduction., 428(19), pp.3752–3775.

**Figure 1**

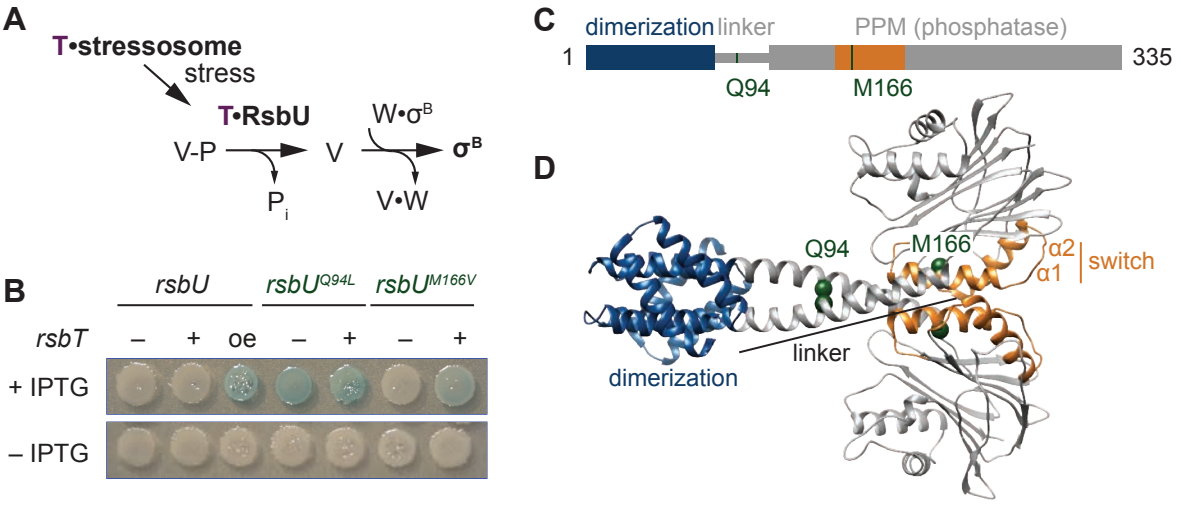
A
T•stressosome
stress
T•RsbU
V-P
V
W•σB
σB
Pi
V•W
B
rsbU
rsbUQ94L
rsbUM166V
rsbT
–
+
oe
–
+
–
+
+ IPTG
– IPTG
C
dimerization
linker
PPM (phosphatase)
1
335
Q94
M166
D
Q94
M166
α2
α1
switch
linker
dimerization

**Figure 1: The linker controls RsbU activation through a conserved switch element**

**A** Reaction scheme of the RsbU dependent pathway of the environmental stress response. RsbU is activated by its partner protein RsbT (T, purple) to dephosphorylate its substrate protein RsbV-P (V-P). This initiates transcription by displacing $\sigma^B$ from inhibition by the anti-sigma factor RsbW (W). **B** Amino acid substitutions in RsbU (Q94L and M166V) cause enhanced $\sigma^B$ activity in *B. subtilis*. Strains carrying a lacZ reporter of $\sigma^B$ activity (*ctc-lacZ*) were plated on X-gal indicator plates in the presence (top) or absence (bottom) of IPTG to induce expression of the rsbU constructs. Strains were deleted for *rsbT* (–) or not (+). A strain overexpressing *rsbT* is indicated by oe. Plates were imaged after 24 hours of growth at 37ºC, which was shorter than the time used to visualize *lacZ* expression from the *rsbU*$^{M166V}$ strain previously (Ho & Bradshaw 2021). **C** Domain diagram of RsbU. The N-terminal domain of RsbU (blue) (amino acids 1-81) is joined to the α-helical linker domain (grey) (82-112), which connects it to the PPM phosphatase domain (grey box) (121-335). The regulatory switch element of the PPM phosphatase domain is colored orange (156-201). The location of RsbT-bypass mutations are highlighted in green. **D** AlphaFold2 model of RsbU dimer. Domains are colored as in C and the Cα atoms of residues Q94 and M166 are shown as spheres.

**Figure 2**

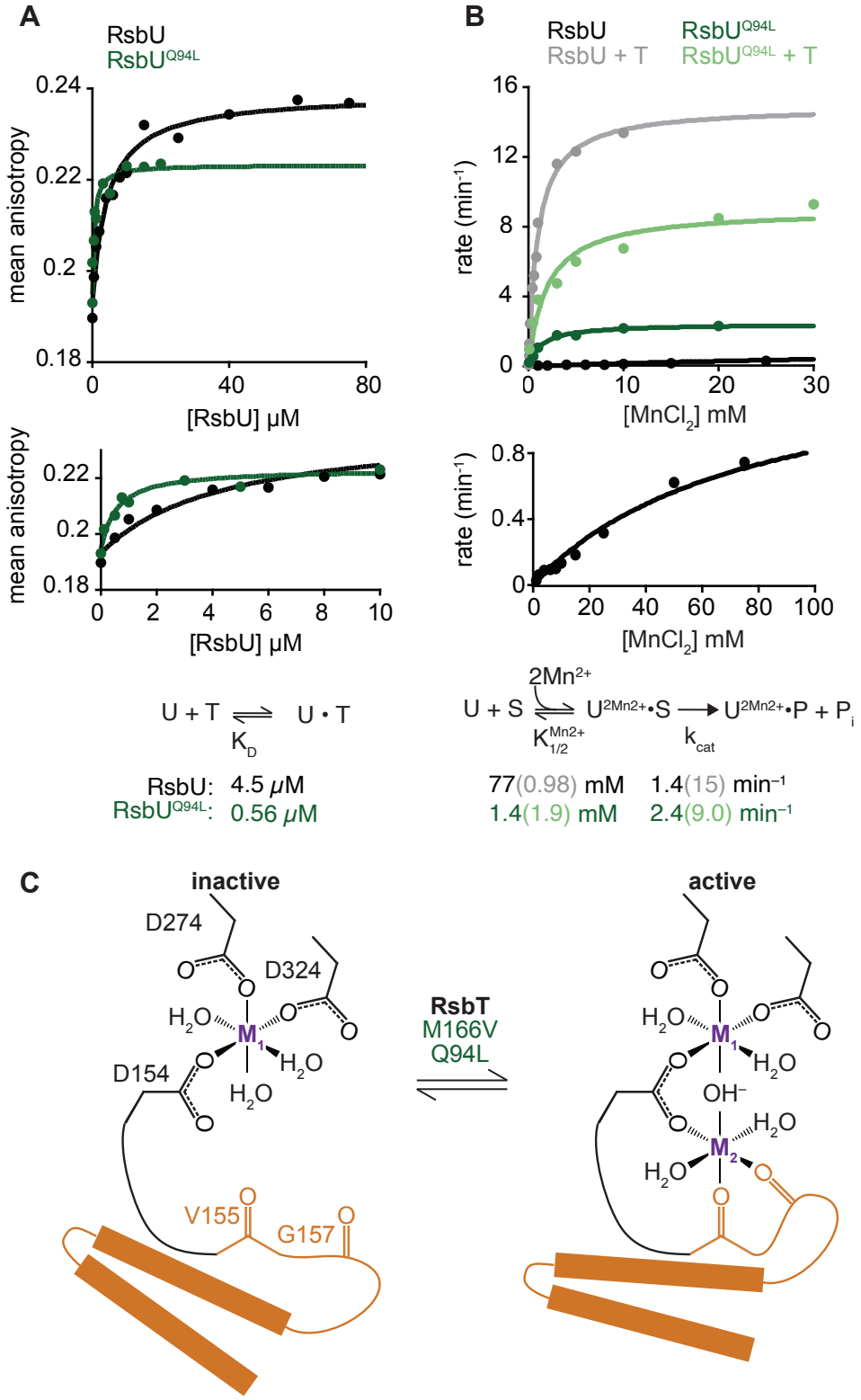
A
RsbU
RsbU^Q94L
mean anisotropy
0.24
0.22
0.2
0.18
0
40
80
[RsbU] μM
0.22
0.2
0.18
0
2
4
6
8
10
[RsbU] μM
B
RsbU
RsbU + T
RsbU^Q94L
RsbU^Q94L + T
rate (min⁻¹)
16
12
8
4
0
10
20
30
[MnCl2] mM
0.8
0.4
0
20
40
60
80
100
[MnCl2] mM
U + T ⇌ U • T
K_D
2Mn2+
U + S ⇌ U2Mn2+•S → U2Mn2+•P + Pi
K_1/2^Mn2+
k_cat
RsbU: 4.5 μM
RsbU^Q94L: 0.56 μM
77(0.98) mM 1.4(15) min⁻¹
1.4(1.9) mM 2.4(9.0) min⁻¹
C
inactive
active
D274
D324
D154
H2O
M1
M2
OH⁻
V155
G157
RsbT
M166V
Q94L

**Figure 2: RsbU linker influences RsbT binding and phosphatase activity**

**A** Mean anisotropy of RsbT-TMR (200 nM) is plotted as a function of RsbU concentration. The curves are fits to a quadratic binding equation using non-linear curve fitting (RsbU (black) $K_D$ = 4.5 ± 0.96 μM, $RsbU^{Q94L}$ (green) $K_D$ = 0.56 ± 0.15 μM). The lower plot shows RsbU concentrations to 10 μM. Below is the reaction scheme of RsbT binding to RsbU with the values for the calculated $K_D$ below. **B** The rate of dephosphorylation of RsbV-P is plotted as a function of concentration of $MnCl_2$ for RsbU (black) and $RsbU^{Q94L}$ (green) in the presence (dark) and absence (light) of RsbT. Curves are fits to the Michaelis-Menten equation using non-linear curve fitting. The $k_{cat}$ of wild-type RsbU is 15 ± 0.35 $min^{-1}$ with RsbT and 1.4 ± 0.077 $min^{-1}$ without RsbT and the $k_{cat}$ of $RsbU^{Q94L}$ is 9.0 ± 0.64 $min^{-1}$ with RsbT and 2.4 ± 0.084 $min^{-1}$ without RsbT. The $K_M^{MnCl2}$ of wild-type RsbU is 0.98 ± 0.069 mM with RsbT and 77 ± 9.0 mM without RsbT and the $K_M^{MnCl2}$ of $RsbU^{Q94L}$ is 1.4 ± 0.19 mM with RsbT and 1.9 ± 0.56 mM without RsbT. The lower plot shows wild-type RsbU in the absence of RsbT for $MnCl^2$ concentrations to 100 mM. Below is a summary of a reaction scheme of RsbU dephosphorylating RsbV-P (denoted as S) with the $K_M^{MnCl2}$ and $k_{cat}$ values below. Data for RsbU are reproduced from (Ho & Bradshaw 2021). **C** A cartoon model of how the switch helices rotate to activate RsbU. Binding of RsbT or mutation moves the switch helices into place during activation to coordinate metal M2. The residues of RsbU that are hypothesized to coordinate metals are shown as sticks (based on homology to RsbX).

**Figure 3**

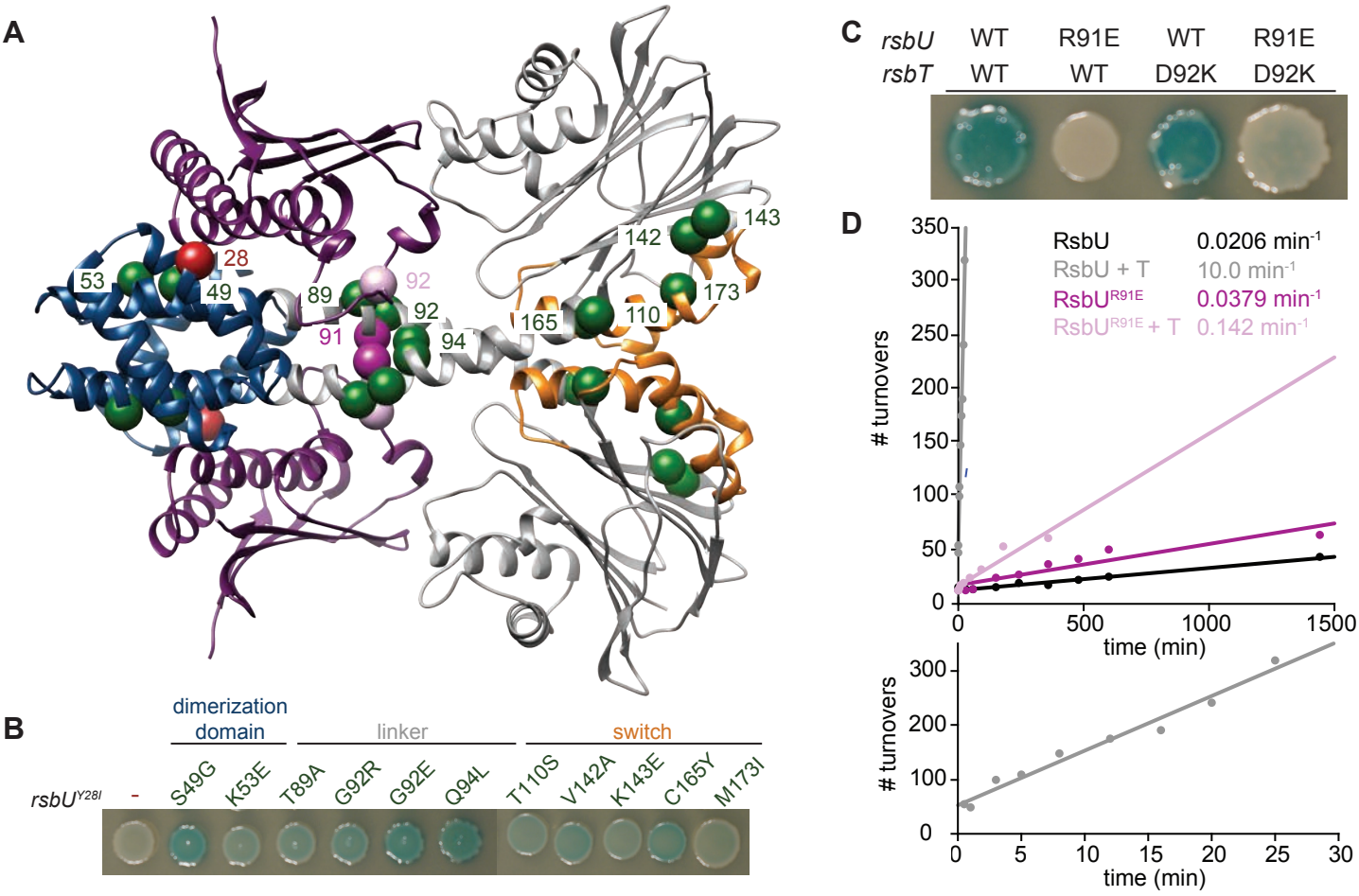
A
28
53
49
89
92
91
92
94
165
110
142
143
173
B
dimerization domain
linker
switch
rsbU^Y28I
-
S49G
K53E
T89A
G92R
G92E
Q94L
T110S
V142A
K143E
C165Y
M173I
C
rsbU WT R91E WT R91E
rsbT WT WT D92K D92K
D
RsbU 0.0206 min-1
RsbU + T 10.0 min-1
RsbU^R91E 0.0379 min-1
RsbU^R91E + T 0.142 min-1
# turnovers
time (min)
# turnovers
time (min)

**Figure 3: RsbT has a hybrid interface with RsbU N-terminal dimerization domain and linker**

**A** An AlphaFold2 model of a heterotetrameric 2RsbT/2RsbU complex is shown in ribbon representation. RsbT (purple) binds with an interface that spans the N-terminal domains (blue) and α-helical linkers (grey) of both RsbU protomers. The PPM phosphatase domains are colored grey and the regulatory switch elements (α1 and α2) are colored orange. The Cα positions of $RsbU^{Y28}$ (red), $rsbU^{Y28I}$ suppressor substitutions (green), $RsbU^{R91}$ (dark pink), and $RsbT^{D92}$ (pink) are shown as spheres with the residue numbers indicated. **B** Strains with a $\sigma^B$ LacZ reporter were plated on IPTG/X-gal plates to induce expression of plasmid borne *rsbT* and *rsbU*$^{Y28I}$ and visualize $\sigma^B$ activity (indicated by blue pigmentation after 24 hours of growth at 37ºC). Additional amino acid substitutions in the *rsbU* gene are indicated above the spots, with the region where they are located in the RsbU structure specified. **C** Strains with indicated changes to the RsbT and RsbU amino acid sequence were plated as in B and plates were imaged after 36 hours of growth at 37ºC. **D** R91E does not decrease the basal phosphatase activity of RsbU. Plots show dephosphorylation of RsbV-P (25 μM) by RsbU (black) and $RsbU^{R91E}$ (pink) (0.5μM) in the presence of 10 mM $MnCl^2$ and the presence or absence of 10 μM RsbT (light colors). Linear fits of the data are shown, with the slopes indicating the observed rates (kobs): RsbU 0.0206 ± 0.00124 $min^{-1}$, RsbU + RsbT 10.0 ± 0.628 $min^{-1}$, $RsbU^{R91E}$ is 0.0379 ± 0.00543 $min^{-1}$, $RsbU^{R91E}$ + RsbT 0.142 ± 0.0161 $min^{-1}$. The lower plot is RsbU in the presence of RsbT to thirty minutes.

**Figure 4**

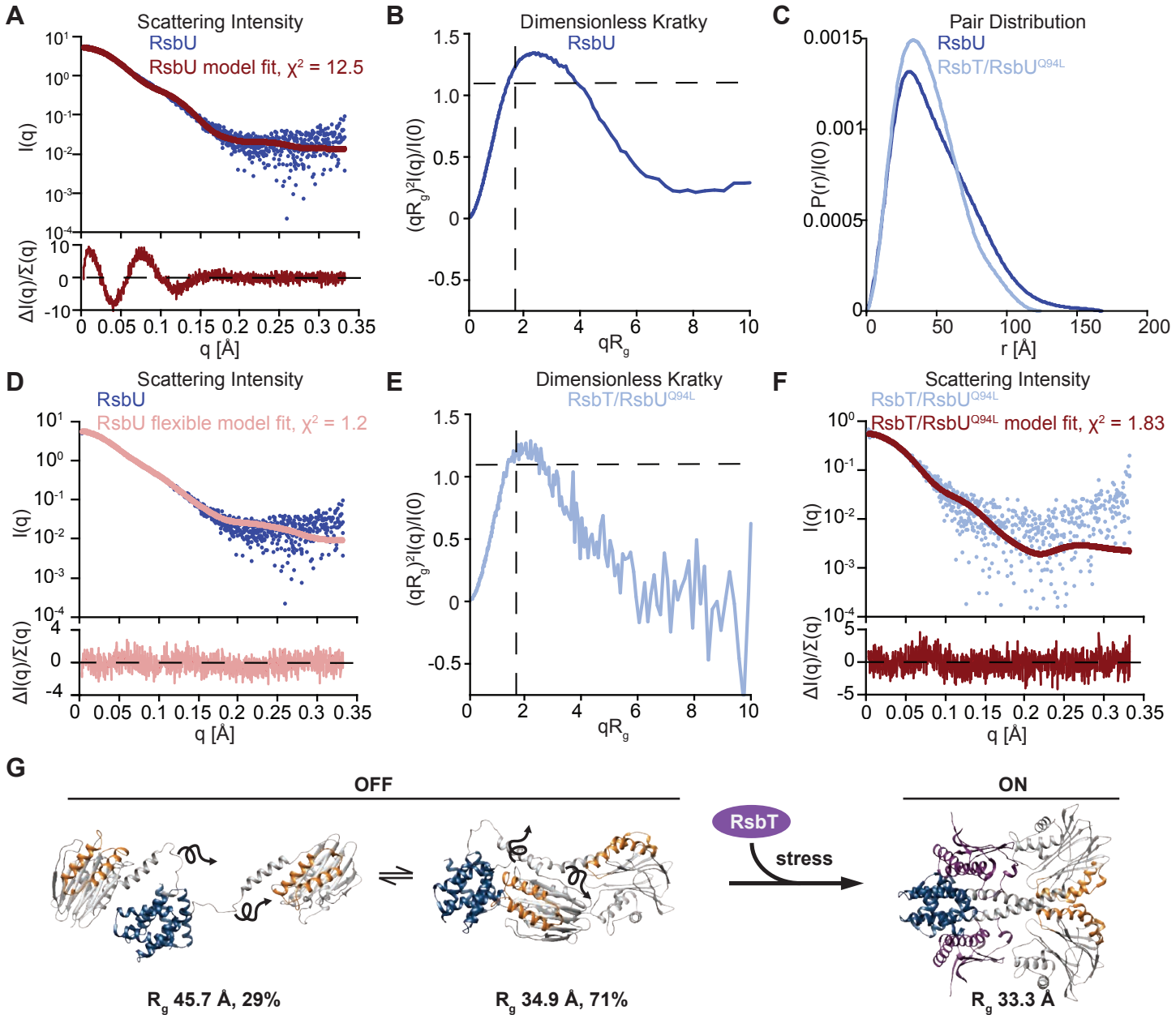
A
Scattering Intensity
RsbU
RsbU model fit, χ² = 12.5
I(q)
ΔI(q)/Σ(q)
q [Å]
B
Dimensionless Kratky
RsbU
(qRg)²I(q)/I(0)
qRg
C
Pair Distribution
RsbU
RsbT/RsbU^Q94L
P(r)/I(0)
r [Å]
D
Scattering Intensity
RsbU
RsbU flexible model fit, χ² = 1.2
I(q)
ΔI(q)/Σ(q)
q [Å]
E
Dimensionless Kratky
RsbT/RsbU^Q94L
(qRg)²I(q)/I(0)
qRg
F
Scattering Intensity
RsbT/RsbU^Q94L
RsbT/RsbU^Q94L model fit, χ² = 1.83
I(q)
ΔI(q)/Σ(q)
q [Å]


G
OFF
ON
RsbT
stress
Rg 45.7 Å, 29%
Rg 34.9 Å, 71%
Rg 33.3 Å

**Figure 4: RsbU linker is flexible in the absence of RsbT, and is rigidified by RsbT binding.**
**A** I(q) versus q plot of the dimer component of SAXS scattering data from RsbU (blue) overlaid with a FoXS generated profile fit of the AlphaFold2 RsbU dimer structure (red). The upper plot shows I(q) versus q on log-linear axes while the lower plot shows the uncertainty normalized residuals of the fit ((experimental-computed)/error), χ2 of 12.53. The AlphaFold2 model used for the fit is shown inset. **B** Dimensionless Kratky plot of SAXS scattering data from the dimer component of RsbU experimental data (blue). The experimental profile was logarthmically binned to reduce noise at high $qR_g$. **C** Normalized P(r) plot from the RsbU dimer (blue) and heterotetrameric RsbT/RsbU$^{Q94L}$ complex (light blue) is shown. **D** I(q) versus q plot of the dimer component of SAXS scattering data from RsbU (blue) is shown overlaid with a MultiFoXS generated two-state profile fit with flexibility allowed for residues 82-96 (pink). The lower plot shows the uncertainty normalized residuals of the fit ((experimental-computed)/error), $\chi^2$ of 1.2. **E** Dimensionless Kratky plot of the heterotetrameric component of RsbT/RsbU$^{Q94L}$ complex is shown binned logarithmically to reduce noise at high $qR_g$ values. **F** I(q) versus q plot of the heterotetrameric component of SAXS scattering data from RsbT/RsbU$^{Q94L}$ complex (blue) overlaid with a FoXS generated profile fit of the AlphaFold2 RsbT/RsbU heterotetramer structure (red). The upper plot show I(q) versus q on a log-linear axes while the lower plot shows the uncertainty normalized residuals of the fits ((experimental-computed)/error), χ2 of 1.83.**G** Schematic of the conformational change of RsbU upon RsbT binding. The two best fit flexible models of RsbU generated from MultiFoXS in panel B are shown with the calculated $R_g$ and percentage of each model used in the fit indicated. These two models are shown in exchange with arrows to indicate flexibility. The AlphaFold2 model of 2RsbU/2RsbT heterotetramer used for the FoXS fit in E is shown with the calculated $R_g$ indicated.

## Figure 5

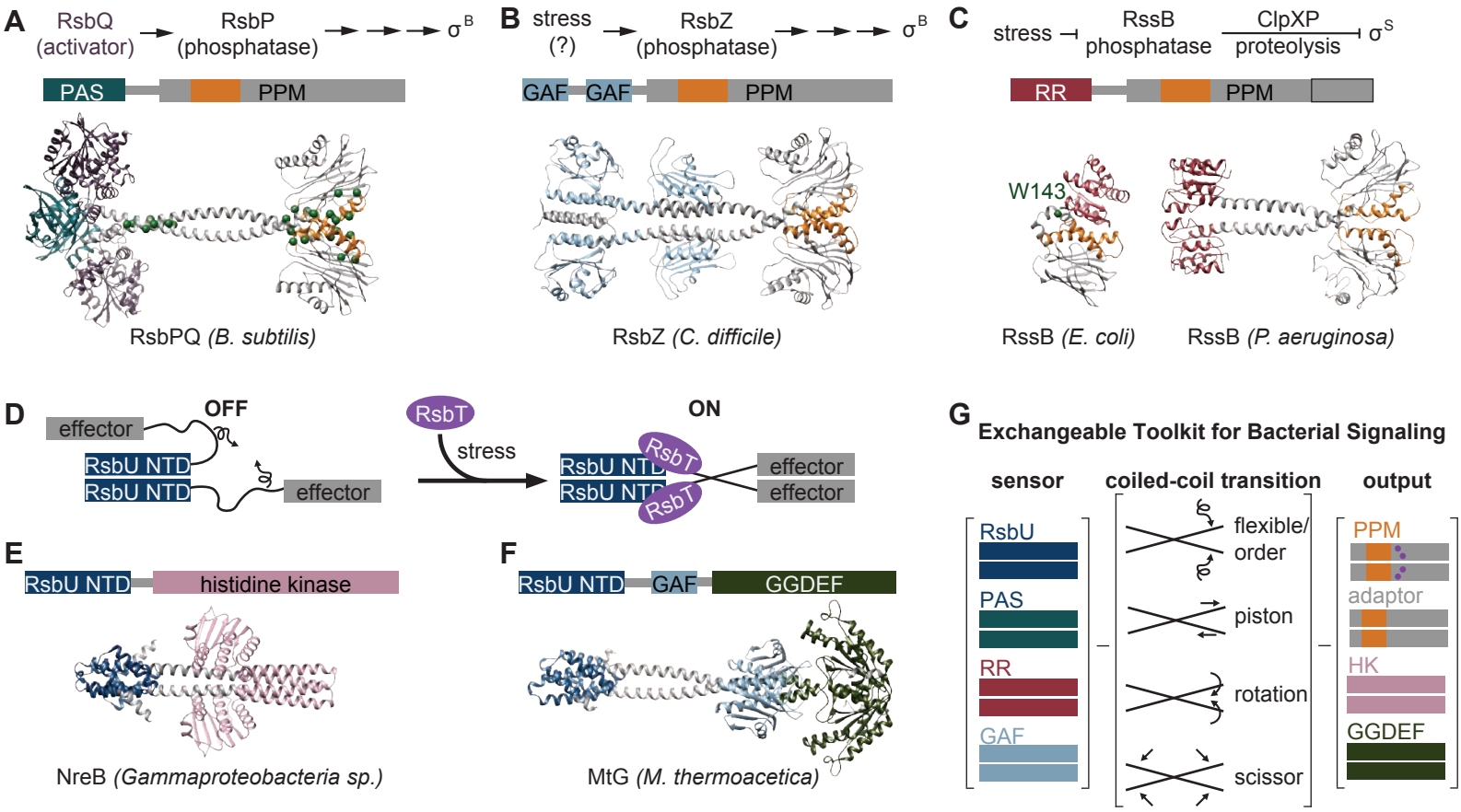
A
RsbQ (activator)
RsbP (phosphatase)
σB
PAS
PPM
RsbPQ (B. subtilis)
B
stress (?)
RsbZ (phosphatase)
σB
GAF
GAF
PPM
RsbZ (C. difficile)
C
stress
RssB phosphatase
ClpXP proteolysis
σS
RR
PPM
W143
RssB (E. coli)
RssB (P. aeruginosa)
D
OFF
effector
RsbU NTD
RsbU NTD
effector
RsbT
stress
ON
RsbU NTD
RsbU NTD
RsbT
RsbT
effector
effector
E
RsbU NTD
histidine kinase
NreB (Gammaproteobacteria sp.)
F
RsbU NTD
GAF
GGDEF
MtG (M. thermoacetica)
G
Exchangeable Toolkit for Bacterial Signaling
sensor
coiled-coil transition
output
RsbU
PAS
RR
GAF
flexible/ order
piston
rotation
scissor
PPM
adaptor
HK
GGDEF

**Figure 5: An exchangeable toolkit for bacterial signal transduction**

**A** An AlphaFold2 model of the *B. subtilis* energy stress phosphatase RsbP is shown bound to its activating α/β-hydrolase protein RsbQ (purple) with a schematic of the σB activation pathway shown above. RsbP has an N-terminal PAS domain (turquoise) that is connected to the PPM phosphatase domain by a predicted coiled coil linker. The Cα positions of bypass suppressor mutations that render RsbP active in the absence of RsbQ(Brody et al. 2009) are shown as green spheres. The switch element of the PPM phosphatase domain (α1 and α2) is colored orange. **B** An AlphaFold2 model of the *C. difficile* GSR phosphatase RsbZ is shown with a schematic of the $\sigma^B$ activation pathway shown above. RsbZ has tandem N-terminal GAF domains (blue) that connect to the PPM phosphatase domain by a predicted coiled coil linker. The switch element of the PPM phosphatase domain (α1 and α2) is colored orange. **C** Experimental structures of the GSR initiating adaptor protein RssB from *E. coli* (left, 8T85) and *P. aeruginosa* (right, 3F7A) are shown with a schematic of the $\sigma^S$ activation pathway shown above. The Cα positions of a bypass suppressor mutation (W143R) that renders RssB insensitive to anti-adapter proteins is shown as a green sphere. The switch element of the PPM phosphatase domain (α1 and α2) is colored orange. The black outline shows the portion of hte PPM phosphatase domain that is missing in the *E. coli* RssB adaptor protein, which lacks phosphatase activity. **D** A cartoon schematic of activation by RsbT of proteins with RsbU NTD through ordering of a flexible linker. The protein is depicted with dimerized RsbU N-terminal dimerization domains (blue) with flexible linkers (black) that extend into two effector domains (grey). During stress conditions, RsbT (purple) activates the protein through binding to hte N-terminal dimerization domains and linkers, rigidifying the linkers to dimerize the effector domains. **E** An AlphaFold2 model of a dimer of the histidine kinase NreB from a *Gammaproteobacteria* species (MBI3545564.1) is shown with the RsbU N-terminal domain colored blue and the histidine kinase domain colored pink. **F** An AlphaFold2 model of a dimer of the GGDEF diguanylate cyclase MtG from *M. thermoacetica* (WP_011392981.1) is shown with RsbU N-terminal domain colored blue, GAF domain colored lite blue, and GGDEF domain colored green. **G** Schematic illustrating how various sensor domains (RsbU N-terminal dimerization domain, PAS, response receiver (RR), and GAF) can control various output activities (serine/threonine phosphatase (PPM), histidine kinase (HK), protease adaptor, and diguanylate cyclase (GGDEF). We hypothesize that the shared regulatory mechanism through a dimeric coiled-coil linker makes these regulatory domains modularly exchangeable across effector domains. Known mechanisms for how allosteric regulation is transmitted through the linker are listed and shown with arrow diagrams.

## Figure 1 - Supplemental Figure 1

### *B. subtilis* RsbU

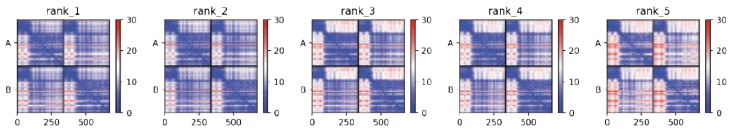


### *B. subtilis* RsbT RsbU

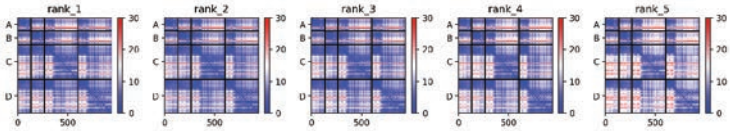


### *B. subtilis* RsbP RsbQ

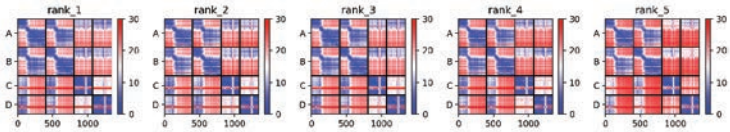


### *C. difficile* RsbZ

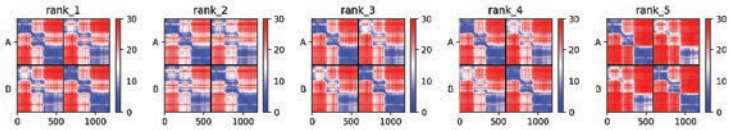


### *Gammaproteobacteria sp.* NreB

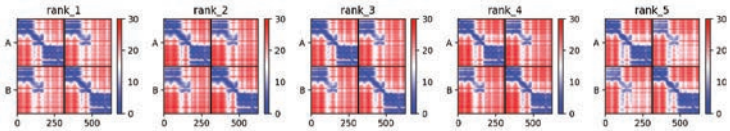


### *M. thermoacetica* MtG

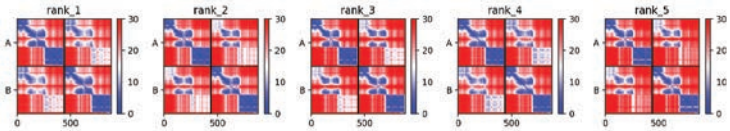


### *M. tuberculosis* Rv1364c

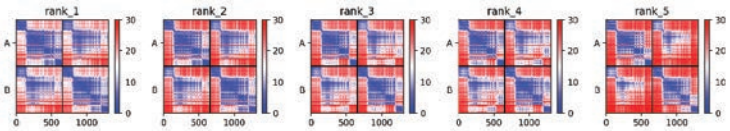


### *S. coelicolor* OsaC

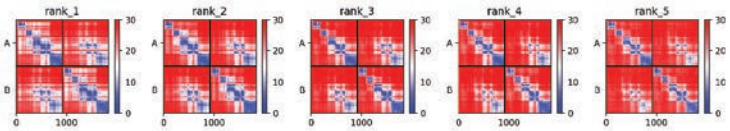


### *R. aetherivorans* WP_029544106.1

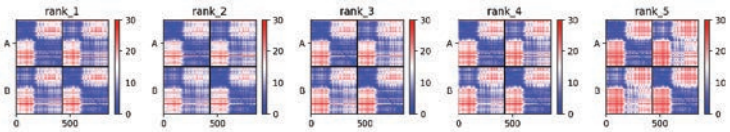


### *S. coelicolor* MYU40396.1

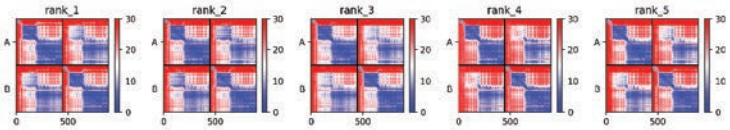


### *Synechocystis sp.* WP_010874143.1

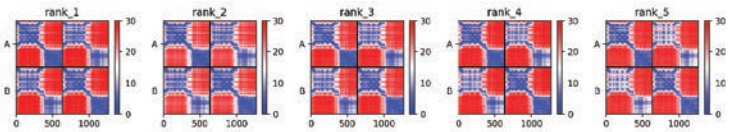

**Figure 1 - Supplemental Figure 1: PAE plots of AlphaFold2 prediction**

Predicted aligned error of the AlphaFold2 structure predictions of the following proteins: B. subtilis RsbU, *B. subtilis* 2RsbT (chains A, B)/2RsbU (chains C,D) complex, *B. subtilis* 2RsbP (chains A,B)/2RsbQ complex (chains C,D), *C. difficile* RsbZ, *Gammaproteobacteria sp.* NreB, *M. thermoacetica* MtG, *M. tuberculosis* Rv1364c, *S. coelicolor* OsaC, *R. aetherivorans* WP_029544106.1, *S. coelicolor* MYU40396.1, and *Synechocystis sp.* WP_010874143.1. Blue indicates high confidence (0 Å) and red indicates low confidence (30 Å).

**Figure 1 - Supplemental Figure 2**

***B. subtilis* RsbU**

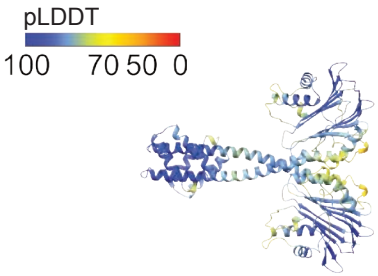


***M. thermoacetica* MtG**

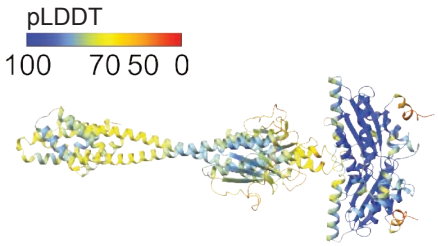


***Synechocystis sp.* WP_010874143.1**

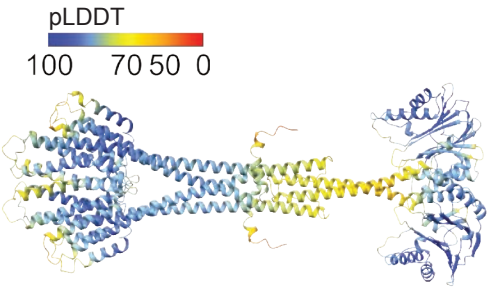


***B. subtilis* RsbT RsbU**

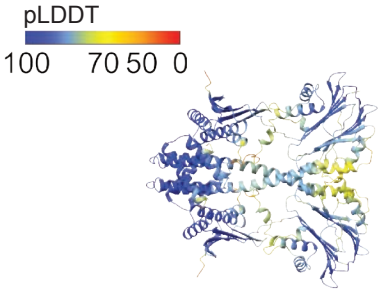


***M. tubercolisis* Rv1364c**

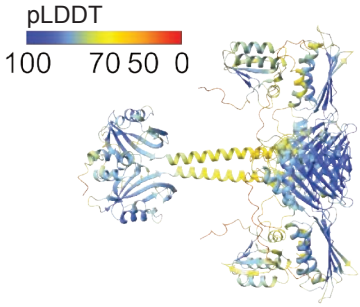


***B. subtilis* RsbP RsbQ**

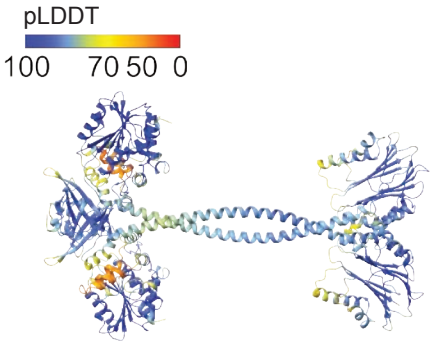


***S. coelicolor* OsaC**

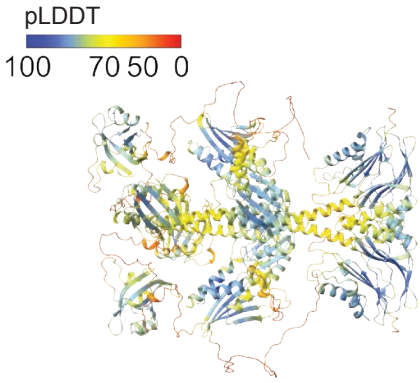


***C. difficile* RsbZ**

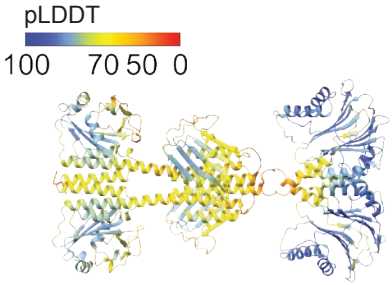


***R. aetherivorans* WP_029544106.1**

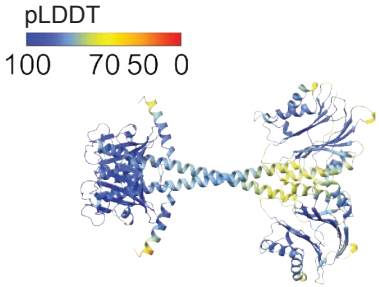


***Gammaproteobacteria sp.* NreB**

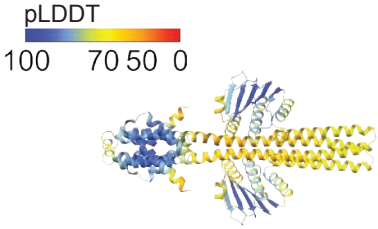


***S. coelicolor* MYU40396.1**

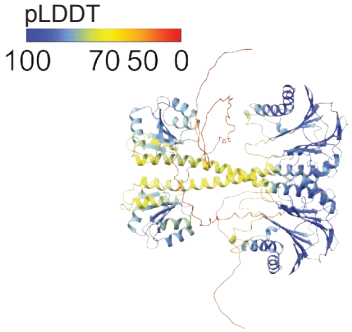

**Figure 1 - Supplemental Figure 2: AlphaFold2 structure predictions with mapped pLDDT scores**

Predicted local distance difference test scores (pLDDT) mapped onto the AlphaFold2 structure predictions of the following proteins: *B. subtilis* RsbU, *B. subtilis* 2RsbT/2RsbU complex, *B. subtilis* 2RsbP/2RsbQ complex, *C. difficile* RsbZ, *Gammaproteobacteria sp.* NreB, *M. thermoacetica* MtG, *M. tuberculosis* Rv1364c, *S. coelicolor* OsaC, *R. aetherivorans* WP_029544106.1, *S. coelicolor* MYU40396.1, and *Synechocystis sp.* WP_010874143.1. The score key is above each structure model. Blue corresponds to a pLDDT score of 90-100 (high confidence), orange to yellow corresponds to a pLDDT score of 50-70 (medium confidence), and red corresponds to a pLDDT score of 0 (low confidence).

**Figure 1 - Supplemental Figure 3**

**A**

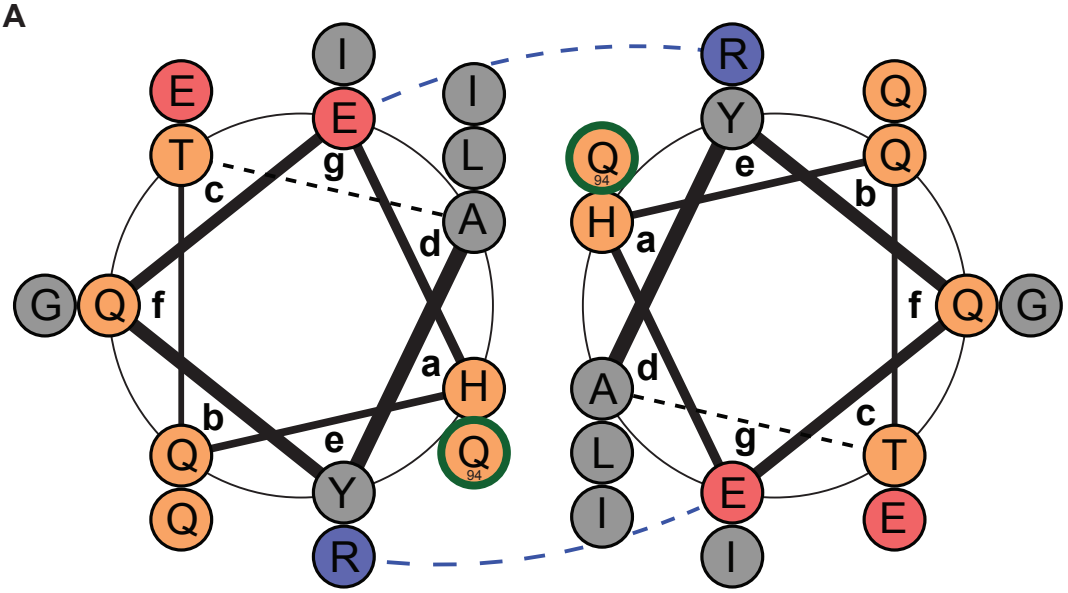


**B**

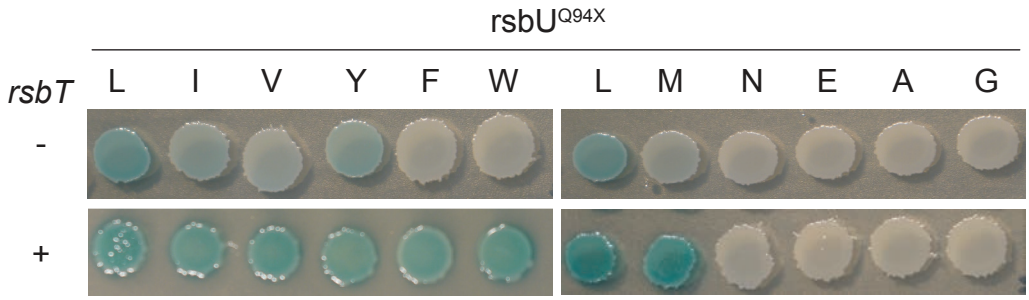


**C**

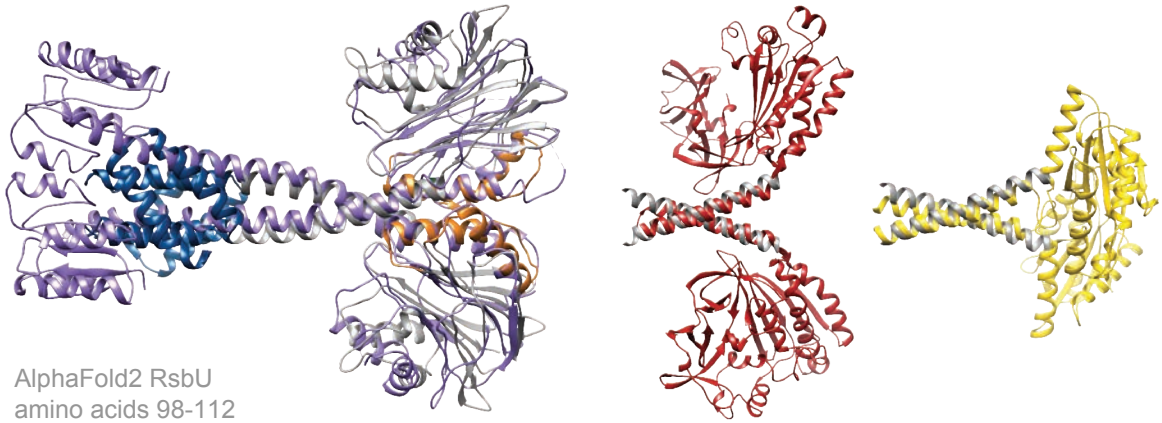

AlphaFold2 RsbU
amino acids 98-112
*P. aeruginosa* RssB
PDB 3F7A
α -18.4°

*T. maritima* CheA
PDB 1B3Q
α -16.8°

*Idiomarina* PadC
PDB 5LLW
α -14.3°

**Figure 1 - Supplemental Figure 3: Q94L stabilizes the packing interface of the coiled-coil of the linker**

**A** Coil diagram of RsbU residues 83-97 generated using DrawCoil. Grey circles indicate non-polar residues, orange indicate polar residues, red indicate negatively charged residues, and blue indicate positively charged residues. The blue dashed line depicts a putative salt bridge. Residue Q94 (circled in green) sits in the interface of the coils and is shown packing with L90. **B** An allelic series of amino acid substitutions at position 94 of RsbU was generated in an *rsbU* expression plasmid. Plasmids were introduced into *B. subtilis* cells containing a LacZ reporter of $\sigma^B$ activity that were deleted for *rsbT* (top) or with *rsbT* retained on the chromosome (bottom). Cells were plated on IPTG/X-gal plates to induce *rsbU* expression and to indicate $\sigma^B$ activity (blue pigmentation). **C** α-helical pitch analysis of coiled-coil domains. The AlphaFold2 model of an RsbU dimer is overlayed with crystal structure of *P. aeruginosa* RssB (PDB 3F7A, purple, left). The helical linker region extending out of the coiled coil (RsbU98-112) is shown (grey) overlaid with *T. maritima* transducing histidine kinase CheA (PDB 1B3Q, red, middle) and *Idiomarina* A28L diguanylyl cyclases PadC (PDB 5LLW, yellow, right). α angles from Crick parameterization analysis using CCCP are shown for the overlaid region.

**Figure 3 - Supplemental Figure 1**

**A**

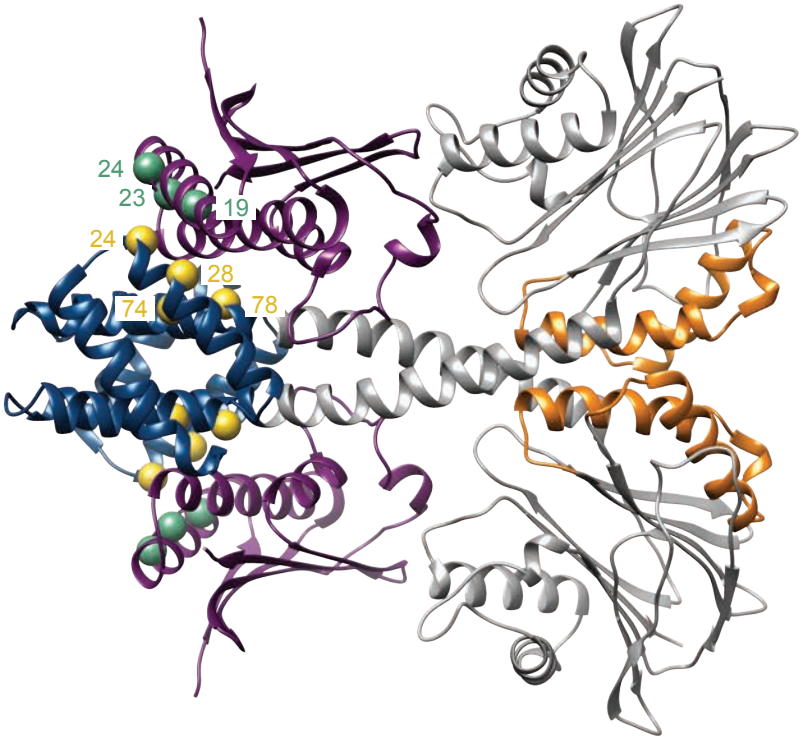

**Figure 3 - Supplemental Figure 1: RsbT binds to the linker**

**A** Interface of RsbT and N-terminal domain of RsbU. A ribbon representation is shown of the AlphaFold2 model of the heterotetrameric 2RsbT/2RsbU complex with RsbU N-terminal dimerization domain colored blue, the switch element of the PPM domain (α1 and α2) colored orange, and RsbT colored purple. The Cα of positions of amino acids implicated in the binding interface of RsbT and RsbU N-terminal dimerization domain (Hardwick et al. 2007) are represented on the AlphaFold2 structure as yellow spheres (RsbU) and green spheres (RsbT) with the residue numbers.

**Figure 4 - Supplemenal Figure 1**

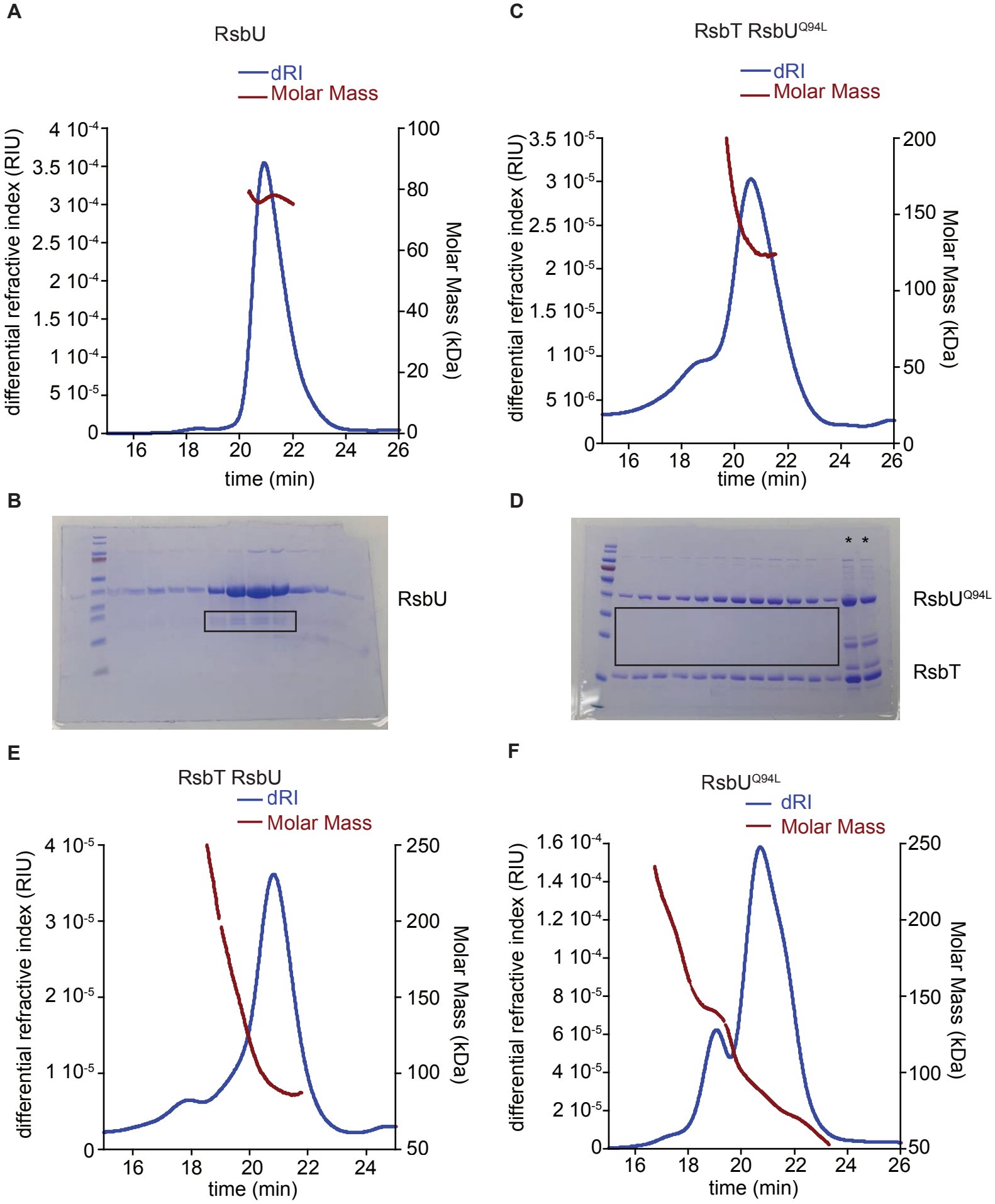

**Figure 4 - Supplemental Figure 1: MALS estimate of molecular weight of RsbU dimer, RsbT/RsbUQ94L complex, RsbT/RsbU complex, and RsbUQ94L**

**A** Plot of inline SEC-MALS analysis of RsbU with measured differential refractive index (blue, left axis) and the molecular weight calculated from MALS (red, right axis). **B** Denaturing SDS-PAGE gel of successive fractions from the equivalent range of the elution as shown in A from preparative size exclusion chromatography of the sample of RsbU used for SEC-MALS-SAXS. Black box denotes the C-terminal truncation product present in each lane of the main peak. **C** Plots from inline SEC-MALS analysis of RsbT/RsbU$^{Q94L}$ complex with measured differential refractive index (blue, left axis) and the molecular weight calculated from MALS (red, right axis). **D** Denaturing SDS-PAGE gel of successive fractions from the equivalent range of the elution of RsbT/U$^{Q94L}$ as shown in C from preparative size exclusion chromatography of the sample used for SEC-MALS-SAXS. Black box denotes lack of C-terminal truncation product during co-expression and purification of RsbT/RsbU$^{Q94L}$ complex. * Denotes load samples on gel. **E** Plots from inline SEC-MALS analysis of RsbT/U complex with measured differential refractive index (blue, left axis) and the molecular weight calculated from MALS (red, right axis). **F** Plot inline SEC-MALS analysis of RsbU$^{Q94L}$ with measured differential refractive index (blue, left axis) and the molecular weight calculated from MALS (red, right axis).

**Figure 4 - Supplemental Figure 2**

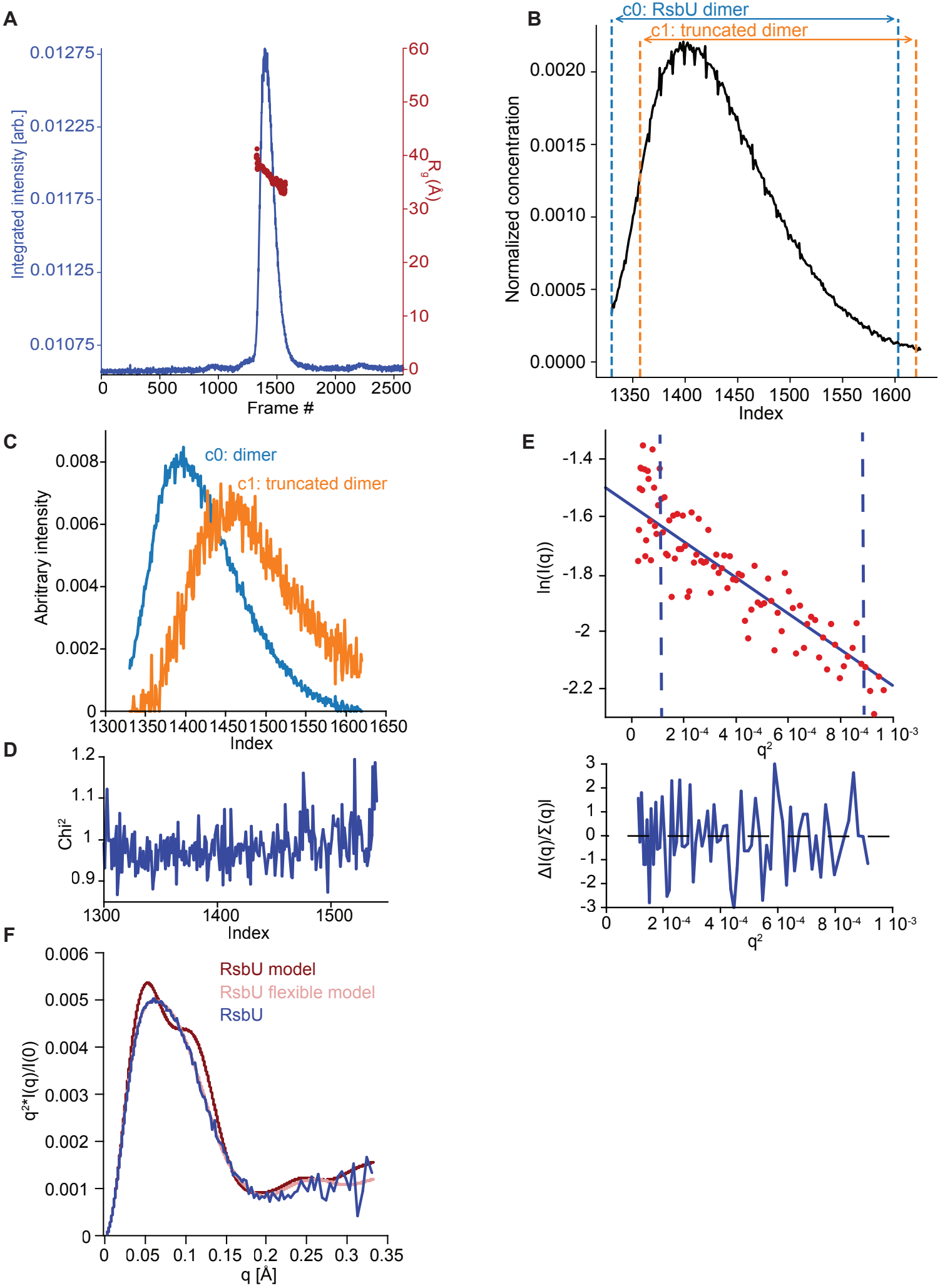

**Figure 4 - Supplemental Figure 2: EFA deconvolution and Guinier analysis of RsbU dimer SAXS profiles**
**A** SAXS data summary for RsbU. Series intensity (blue, left axis) versus frames, and $R_g$ versus frame (red, right axis) are plotted. **B** The selected intensity range for EFA (black) (frame index 1330-1620), and the individual component ranges for deconvolution; blue denotes the range of frames where the scattering component we assigned as the c0, RsbU dimer, was detected (frame index 1330-1603) and orange denotes the range of frames where the scattering component that is c1, presumably from a RsbU heterodimer containing a c-terminal truncation product dimer (frame index 1357-1620). **C** Area normalized concentration profiles for the c0, RsbU dimer component (blue) and c1, RsbU heterodimer containing c-terminal truncation product dimer (orange). **D** Mean $\chi 2$ values for the fit of the EFA deconvolution to the original scattering data. **E** Guinier fit for RsbU dimer component on the upper plot and uncertainty normalized residuals of the fit on the lower plot. The scattering data for the dimer component (red) is fit to the Guinier approximation (blue). The blue dashed lines are the $q_{min}$ and $q_{max}$ at values 0.00356 Å-1 and 0.0234 Å-1, respectively. **F** Kratky plot of SAXS scattering data from the dimer component of RsbU experimental data (blue) overlaid with the profile computed by FoXS based on the AlphaFold2 model of an RsbU dimer (red) and the profile of the flexible model computed by MultiFoXS (pink). The experimental profile was logarthmically binned to reduce noise at high q.

**Figure 4 - Supplemental Figure 3**

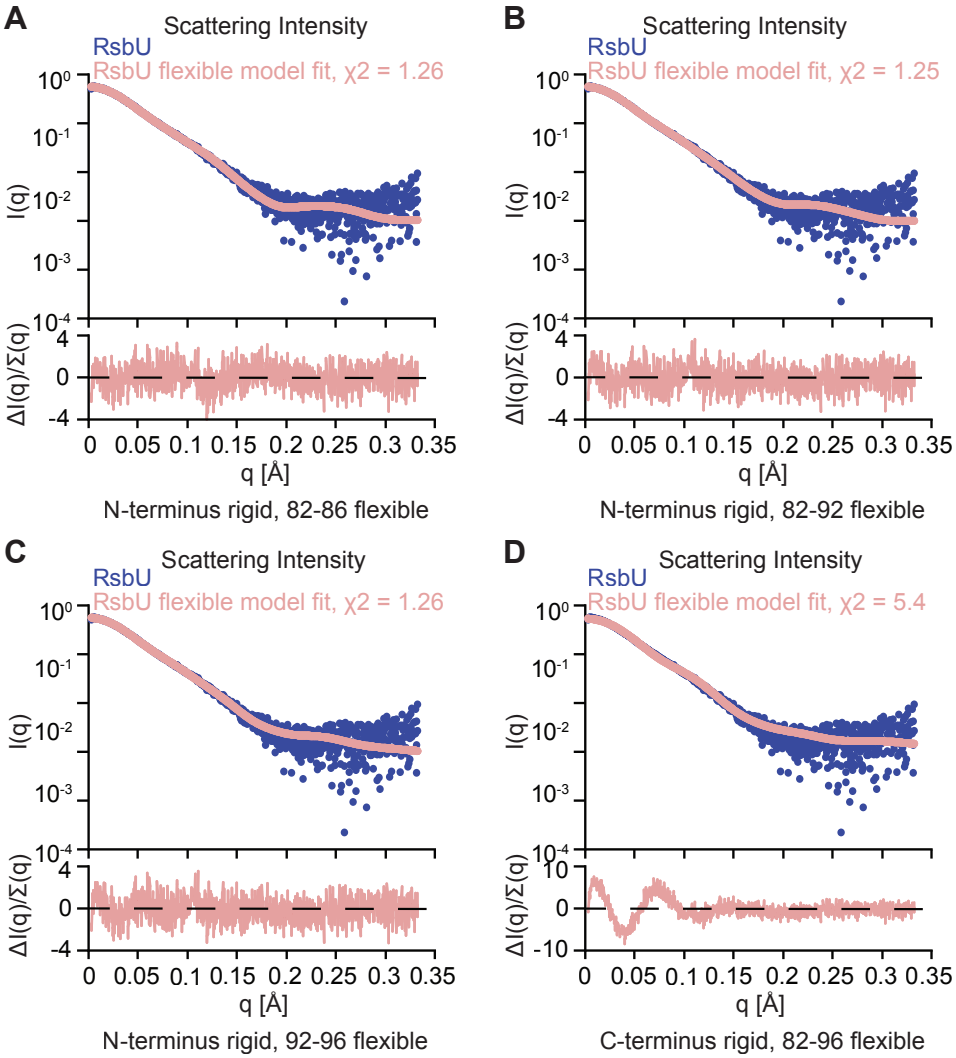

**Figure 4 - Supplemental Figure 3: Varying constraints and flexibility of RsbU model**

**A** I(q) versus q plot of the dimer component of SAXS scattering data from RsbU (blue) overlaid with a MultiFoXS generated two-state profile fit with flexibility allowed for residues 82-86 (pink). The upper plot shows I(q) versus q on log-linear axes while the lower plot shows the uncertainty normalized residuals of the fit ((experimental-computed)/error), $\chi^2$ of 1.26. **B** I(q) versus q plot of the dimer component of SAXS scattering data from RsbU (blue) overlaid with a MultiFoXS generated two-state profile fit with flexibility allowed for residues 82-92 (pink). The upper plot shows I(q) versus q on log-linear axes while the lower plot shows the uncertainty normalized residuals of the fit ((experimental-computed)/error), $\chi^2$ of 1.25. **C** I(q) versus q plot of the dimer component of SAXS scattering data from RsbU (blue) overlaid with a MultiFoXS generated two-state profile fit with flexibility allowed for residues 92-99 (pink). The upper plot shows I(q) versus q on log-linear axes while the lower plot shows the uncertainty normalized residuals of the fit ((experimental-computed)/error), $\chi^2$ of 1.26. **D** I(q) versus q plot of the dimer component of SAXS scattering data from RsbU (blue) overlaid with a MultiFoXS generated two-state profile fit with flexibility allowed for residues 82-96 (pink) and the C-terminal domains constrained. The upper plot shows I(q) versus q on log-linear axes while the lower plot shows the uncertainty normalized residuals of the fit ((experimental-computed)/error), $\chi^2$ of 5.4.

**Figure 4 - Supplemental Figure 4**

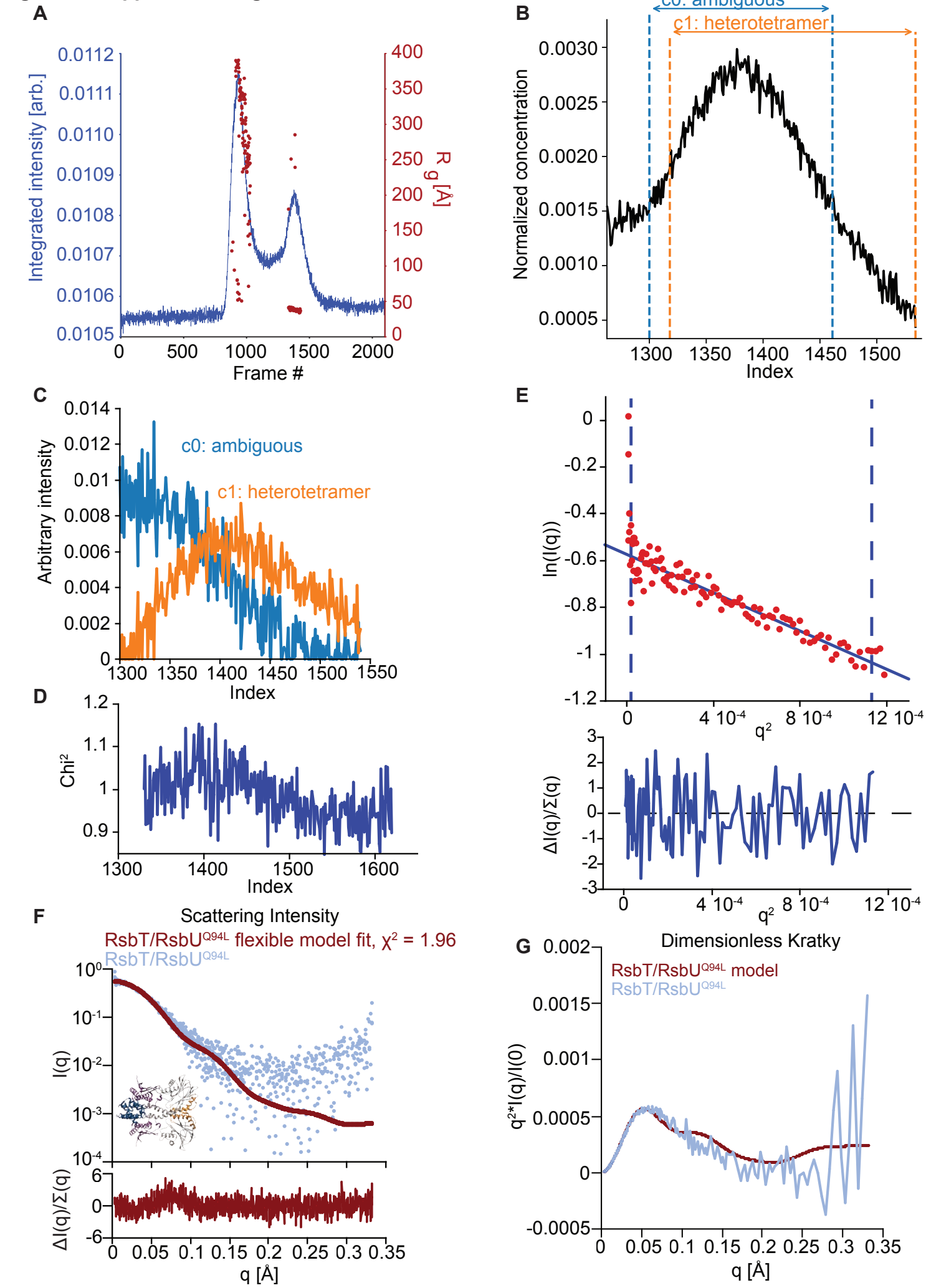

**Figure 4 - Supplemental Figure 4: EFA deconvolution and Guinier analysis of RsbT/RsbU$^{Q94L}$ SAXS profiles**

**A** SAXS data summary for RsbT/RsbU$^{Q94L}$. Series intensity (blue, left axis) versus frames, and $R_g$ versus frame (red, right axis) are plotted. **B** The selected intensity range for EFA (black) (frame index 1300-1540), and the individual component ranges for deconvolution; blue denotes the range of frames where the scattering component we assigned as c0, ambiguous component, was detected (1300-1461) and orange denotes the range of frames where the scattering component we assigned as c1, the 2RsbT/2RsbU$^{Q94L}$ heterotetrametric complex, was detected (1318-1540). **C** Area normalized concentration profiles for 2RsbT/2RsbU$^{Q94L}$ heterotetrameric complex (orange) and ambiguous component (blue). D Mean $\chi^2$ values for the EFA deconvolution fit to the original scattering data. **E** Guinier fit for 2RsbT/2RsbU$^{Q94L}$ heterotetrameric complex component on the upper plot and uncertainty normalized residuals of the fit on the lower plot. The scattering data for the dimer component (red) is fit to the Guinier approximation (blue). The blue dashed lines are the $q_{min}$ and $q_{max}$ at values 0.0033 Å$^{-1}$ and 0.0336 Å$^{-1}$, respectively. **F** I(q) versus q plot of the heterotetrameric complex component of SAXS scattering data from 2RsbT/2RsbU (blue) overlaid with a MultiFoXS generated two-state profile fit with flexibility allowed for residues 82-96 (red). The upper plot shows I(q) versus q on log-linear axes while the lower plot shows the uncertainty normalized residuals of the fit ((experimental-computed)/error), $\chi^2$ of 1.96. The one-state flexible model is shown with a RMSD to the AlphaFold2 prediction of 2RsbT/2RsbU of 1.36 Å. **G** Kratky plot of SAXS scattering data from the heterotetrameric component of 2RsbT/2RsbU experimental data (blue) overlaid with the profile computed by FoXS based on the AlphaFold2 model of an RsbT/RsbU heterotetramer (red). The experimental profile was logarithmically binned to reduce noise at high q.

# Figure 5 - Supplemental Figure 1

**A** *M. tuberculosis* Rv1364c

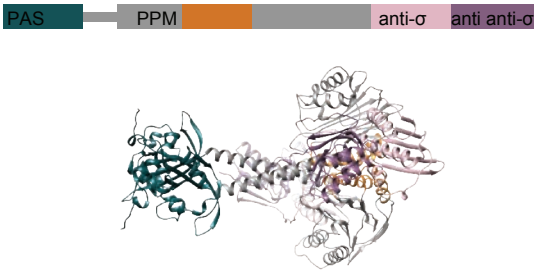


**B** *S. coelicolor* OsaC

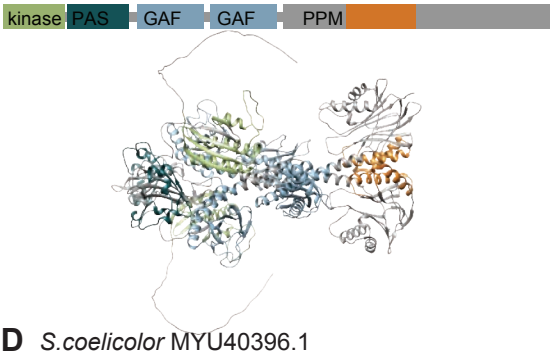


**C** *R. aetherivorans* WP_029544106.1

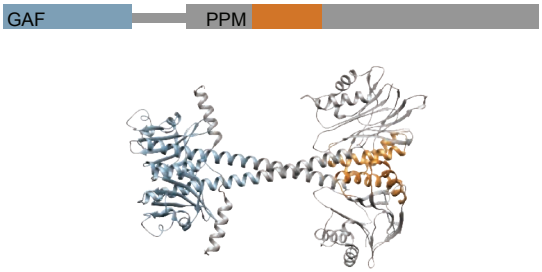


**D** *S.coelicolor* MYU40396.1

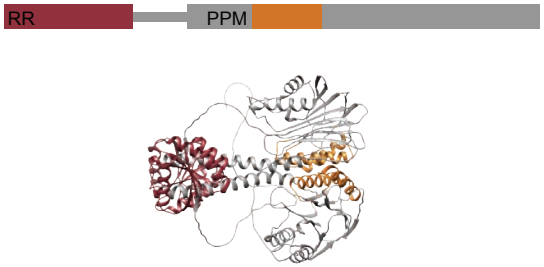


**E** *Synechocystis sp.* WP_010874143.1

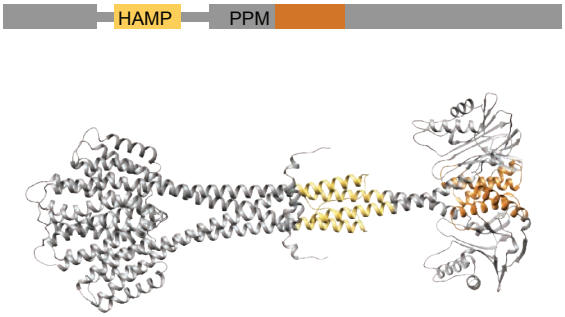

**Figure 5 - Supplemental Figure 1: AlphaFold2 predictions of varying signaling PPM phosphatases**

**A** An AlphaFold2 model of the *M. tubercolisis* GSR phosphatase Rv1364c is shown with a N-terminal PAS domain colored turquoise that connects to the PPM phosphatase domain colored grey, an anti-σ domain (related to RsbW) colored pink and an anti-anti-σ domain (related to RsbV) colored purple. The switch element of the PPM phosphatase domain (α1 and α2) is colored orange. **B** An AlphaFold2 model of the *S. coelicolor* OsaC GSR phosphatase is shown with a N-terminal RsbW-like kinase domain colored in green, connected to a PAS domain colored in turquoise, tandem GAF domains colored in blue, and a PPM phosphatase colored in grey. The switch element of the PPM phosphatase domain (α1 and α2) is colored orange. **C** An AlphaFold2 model of a dimer of the phosphatase from *R. aetherivorans* (WP_029544106.1) is shown with the GAF domain colored in blue connected to the PPM phosphatase colored in grey. The switch element of the PPM phosphatase domain (α1 and α2) is colored orange. **D** An AlphaFold2 model of a dimer of the phosphatase from *S. coelicolor* (MYU40396.1) is shown with the response receiver domain colored in red connected to the PPM phosphatase colored in grey. The switch element of the PPM phosphatase domain (α1 and α 2) is colored orange. **E** An AlphaFold2 model of a dimer of the phosphatase from *Synechocystis species* (WP_010874143.1) is shown with the HAMP domain colored in yellow connected to the PPM phosphatase colored in grey. The switch element of the PPM phosphatase domain (α1 and α2) is colored orange. The structure models in all panels are shown aligned by the top PPM domain to highlight the conservation of the PPM dimer in predictions of dimeric phosphatases with diverse regulatory domains.

## Figure 5 - Supplemental Figure 2

**A**

*B. subtilis* RsbPQ

d a d a d a d a d a d a

126 AQEALLA**K**QKA**N**AELEIALETLKAK**Q**EELLEI**N**KQ**N**QQF**K** 165

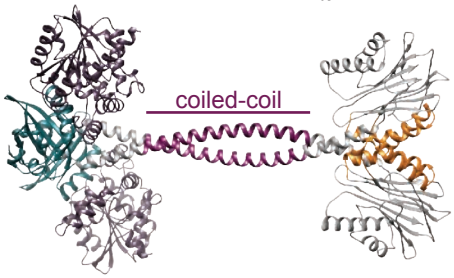


**B**

*C. difficile* RsbZ

d a d a d

182 VQILIDKLRGSISAI 196

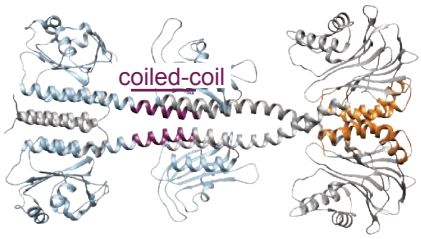


**C**

*P. aeruginosa* RssB

d a d a d a d a

127 LRVE**N**QR**Y**RDKLEAANRELQA**S**LNLL 152

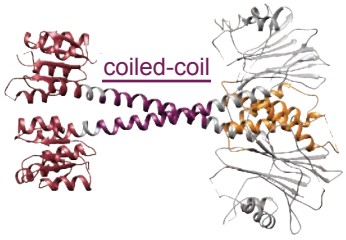


**D**

*Gammaproteobacteria* NreB

a d a d a

94 T**H**RS**Y**REA**N**GALHRL**N**E 110

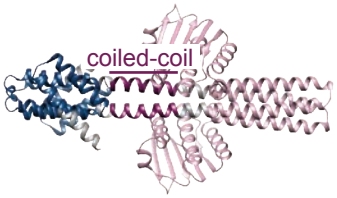


**E**

*M. thermoacetica* MtG

a d a d a d

244 **Y**AALAIE**R**ARLYEAMKF**Q** 261

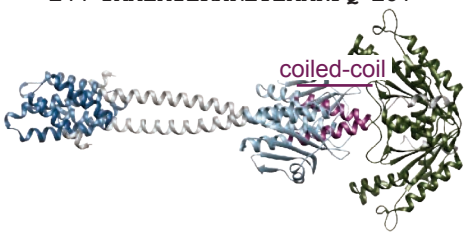


**F**

*M. tuberculosis* Rv1364c

d a d a d a d

140 AEARVEELSER**Y**RNVRDSATVM 161

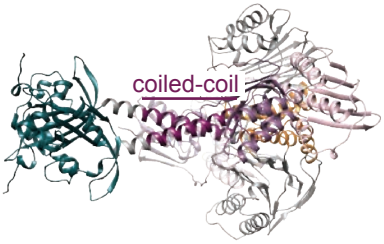


**G**

*S. coelicolor* OsaC

*No coiled-coil*

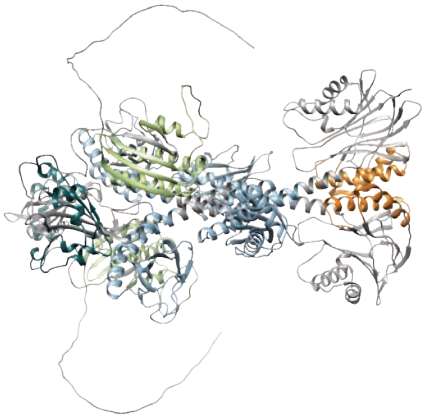

**H**

*R. aetherivorans* WP_029544106.1

d a d a d a d a d a

161 LRLSALA**T**VRA**E**RDLRLQAER**D**RHVLAELATTL 193

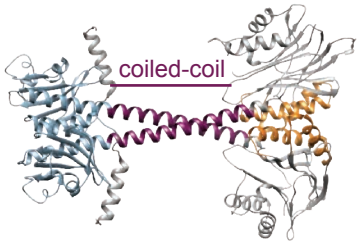


**I**

*S.coelicolor* MYU40396.1

a d a d a d

189 AEQAAVALQA**S**QMQAQE**N** 206

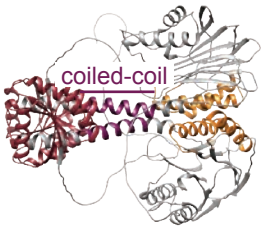


**J**

*Synechocystis sp.* WP_010874143.1

a d a d a da d a

367 FNTVADALCRLTEKLQD**EN**LRLEAEI 392

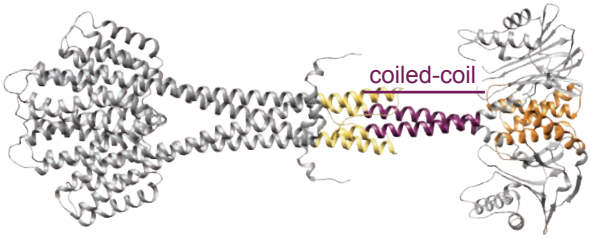

**Figure 5 - Figure Supplement 2: Coiled-coil analysis of structures of bacterial signaling enzymes**

Models of selected phosphatases are shown: **A**, heterotetramer of RsbPQ from *B. subtilis*; **B**, RsbZ from *C. difficile*; **C**, RssB from *P. aeruginosa* (PDB: 3EQ2); **D**, NreB from *Gammaproteobacteria*; **E**, MtG from *M. thermoacetica*; **F**, Rv1364c from *M. tuberculosis*; **G**, OsaC from *S. coelicolor*; **H**, WP_029544106.1 from *R. aetherivorans*; **I**, MYU40396.1 from *S. coelicolor*; **J**, WP_010874143.1 from *Synechocystis sp.*. Coiled-coil sequences identified by Socket2 are shown above the model with the non-polar positions of a and d shown in pink above the sequence. Polar residues at the a and d positions are in bold. The coiled-coil region on the model is shown in pink, the switch helices of the PPM domains are shown in orange, and the various regulatory domains are shown in the following colors: RsbU NTD (blue), PAS (green), GAF (light blue), response receiver (red), and HAMP (yellow).